Mathematisches Forschungsinstitut Oberwolfach

The Mathematics of Mechanobiology and Cell Signaling

Organised by
Davide Ambrosi, Milano
Chun Liu, Chicago
Matthias Röger, Dortmund
Angela Stevens, Münster

25 February – 3 March 2018

ABSTRACT. The workshop focussed on the mathematical modeling and analysis of the mutual interaction among living cells, their interaction with the environment, and the resulting morphogenetic processes. The interplay of bio-mechanical processes and molecular signaling and their combined effect on the emergence of shape and function in cell clusters, tissues, and organs was addressed. Classical methods of continuum mechanics and necessary extensions were discussed at a formal and a rigorous mathematical level. Several introductory talks were given by experimentalists.

Introduction by the Organisers

In the last decade there is an emerging experimental evidence that cells do not only communicate on the basis of bio-chemical signals, but also respond to mechanical stimuli, possibly produced by the cells themselves. A large number of morphogens and soluble factors diffuse and are degraded in living matter. Cells determine their migration, proliferation rate and possibly their fate on the basis of such patterns. In the same vein, mechanical solicitations, stress and variation of the physical properties affect and possibly determine developmental processes, physiology and disease states in cells and tissue.

Mathematical Biology has intensively dealt with the modeling and analysis of diffusive signaling and its interplay with cell proliferation and motion, e.g. via reaction-drift-diffusion-models and transport-type equations. So far, much less

focus has been on the mathematics of models which take into account mechanical forces and more localized signaling processes.

Major questions that are currently debated are how chemical signals and molecular information is translated into a controlled mechanical response of cells and tissues and vice versa, i.e. what are the functional mechanism of mechanotransduction. In higher organisms every living cell is embedded into a complex and dynamic environment which consists of molecular bound and soluble factors, of the extracellular matrix (ECM) and other cells. Cell function and morphology are strongly regulated by these factors. The microenvironment of a single cell does trigger responses like cell proliferation, differentiation and migration and thus, on the large scale, drives processes like morphogenesis and development. Mechanical and chemical information from the outside of a cell not only translates into chemical and mechanical information inside the cell, but also vice versa.

Active single cell mechanics changes the structure of the cell's surrounding environment, produces contact interactions with neighboring cells and with the ECM. Such signals, the mechanical compliance of the ECM and that of adjacent cells then feed back into single cell tension, adhesion, gene and protein expression, the enzymatic modification of proteins after biosynthesis, cell viability, and cytoskeletal organization - one of the main intracellular structural components.

How living cells exactly sense their environment and react with defined responses in terms of morphology, migration, proliferation, cell death, or cell differentiation are questions of actual and major importance in cell biology.

The mechanobiology of living soft matter is a research field where the formulation and analysis of suitable mathematical models is still in its infancy. Therefore this workshop gathered promising young researchers and senior specialists from biomathematics, biophysics, mathematical modeling, partial differential equations, calculus of variations, mathematical material sciences and engineering.

A few central talks were given by biologists at the beginning of the workshop. Their contributions covered experimental results on tissue flows in chicken embryos, self-organization in mouse development, mechanotransduction by ECMs, and adhesion-independent migration of cells. A further interest was, how to best characterize plasma membrane cholesterol. Finally, the particular challenges of mathematical modeling of life science applications were addressed.

From the modeling and computational point of view models for organogenesis were introduced, models for cell migration and proliferation with mechanical and biochemical interactions, as well as models for ion transport. On the level of tissues important topics for mathematical modeling and analysis were the peculiarities of the brain in comparison to other tissues, glioma growth, and tumor invasion through the basal membranes. Further, the mathematical description of early stages of atherosclerosis was presented, and models for T-cell signaling. After an overview of forces in biosysems, bio-mechanical models and their analysis was covered by presentations on multiphase models for tissues, tissue self-organization

through mechanical feedback, multiscale modeling of biomechanics and signaling in plants, force generation and contraction in the cellular cytoskeleton, and cell crawling without adhesion. Mathematical methods of importance in these contexts were discussed in talks about indentation of spherical shells, pattern generating mechanisms, and pattern formation through growth, as well as in talks about unbalanced optimal transport and on a Hamilton-Jacobi approach for the evolution of phenotypically structured (cell) types in time-varying environments. The dynamics of fluidic two-phase biomembranes was analyzed and the wrinkling in a bidomain model, which is relevant for the electrical properties of intra- and extracellular media, separated by a cellular membrane. The homoenergetic solutions presented for the Boltzmann equation are relevant for the dynamics of open systems, which exchange matter, energy or momentum with an "outside" environment.

Two discussion sessions were spontaneously organized. On the second day of the workshop a lively discussion with the experimentalists took place. This allowed for detailed questions, especially of young mathematicians, about important experimental insights which have to be taken into account for reliable mathematical modeling. Later, there was a discussion session about promising recent mathematical techniques, especially from mathematical material sciences. These methods may be relevant for the further development of a sound continuum mechanics for soft tissues.

It was a great pleasure for us to organize this workshop, and we would like to express our sincere thanks to the Oberwolfach team for the professional and very kind support before and during our stay at MFO.

Workshop: The Mathematics of Mechanobiology and Cell Signaling

Table of Contents

Abstracts

Cellular mechanism driving the tissue flows during the formation of the primitive streak in the chick embryo

Cornelis J. Weijer

Gastrulation is a key process during the early embryonic development of all higher organisms. During gastrulation the three germlayers, the ectoderm, mesoderm and endoderm take up their correct topological positions in the embryo, with the ectoderm on the outside, the mesoderm in the middle, surrounding a central layer the endoderm. The ectoderm will give rise to the skin and nervous system, the mesoderm will give rise to the muscles and skeleton as well contribute to many critical organs such as the heart, lungs, kidneys the digestive system and the blood vessels and organs of the immune system. The endoderm will form the lining of the digestive tracks and many associated organs. In amniotes including humans the mesendoderm precursors ingress through a structure known as the primitive streak [1]. The formation of primitive streak is studied extensively in chick embryos as a model for early human embryonic development. Formation of the streak involves millimetre scale tissue flows. We investigate the cellular mechanisms that drive these tissue flows and the mechanisms that integrate these cell behaviours during streak formation. At the time of egg laying the chick embryo consist of a single epithelial layer of cells, the epiblast. The epiblast contains already around 50000 cells and is also known as the Area Opaca. The embryo is surrounded by a ring of extraembryonic tissue, known as the Area Pellucida. During the early stages of development some scattered epiblast cells ingress into the embryo to form the hypoblast, a transient layer that fulfils an important signalling function during development. During gastrulation in the chick embryo the epiblast reorganises to form two additional layers of cells: the mesoderm and the endoderm. Precursors of these cells so called mesendoderm cells are induced in the epiblast by signals originating in the posterior extraembryonic region. These precursor cells are arranged in a sickle shaped region in the posterior side of the embryo. During the early stages of gastrulation these mesendoderm cells move in two large scale vortex flows towards the midline of the embryo forming the primitive streak [2]. The primitive streak is the structure where the mesendoderm cells undergo an epithelial to mesenchymal transition and ingress into the embryo to form the mesoderm and endoderm. We investigate the cellular mechanisms that drive these large scale movements in the epiblast. We take advantage of a novel transgenic chick strain in which all cell membranes are labelled with GFP. To visualise the behaviour of the cells in the epiblast we have developed a dedicated lightsheet microscope that allows us to visualize detailed behaviours such as cell division, cell shape change and relative cell movements such as cell-cell intercalations. Quantitative analysis of the tissue flow patterns show that the mesendoderm region is characterised by a large strain rate. We have furthermore developed algorithms to segment and to track over 200.000 cells in the epiblast, which allows us to monitor

in vivo cell shape changes, cell division and cell movement. Analysis of the cell behaviours show that streak formation is mainly driven by two cellular processes: apical contraction and ingression of mesendoderm cells and myosin dependent directional contractions of cell junctions resulting in directional cell-cell intercalation contributing to expansion along the primitive streak (fig 1).
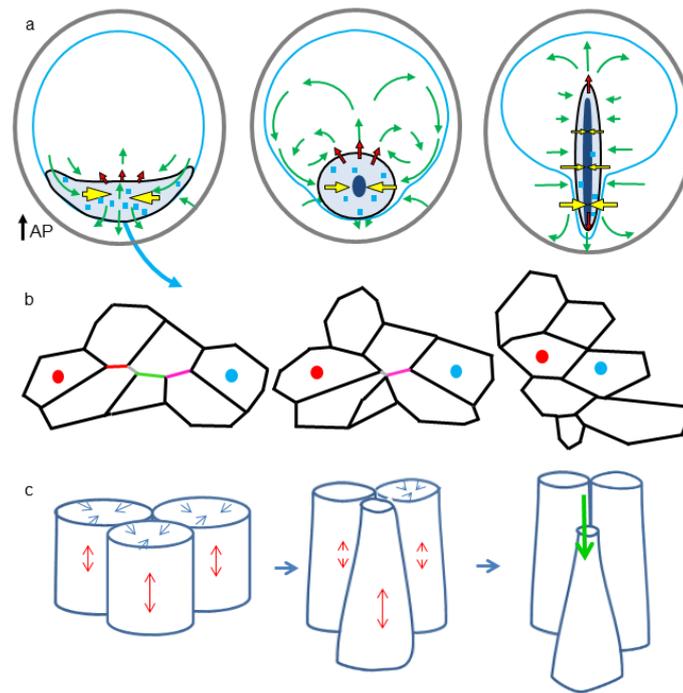
FIGURE 1. Model of the forces and cell behaviours controlling streak formation. **a-)** Diagrams depicting forces generating the tissue flows during streak formation. The active pulling forces - yellow arrows, the passive pushing forces - red arrows, the direction of tissue flows - green arrows. The sickle region is indicated in black, the Area Pellucida outline in blue. Light blue squares indicate scattered events of junctional contraction, while dark blue shapes indicate regions of ingression. **b-)** Schematic of sequential junctional contraction (in a region marked by the blue squares in A). The sequentially contracting junctions are indicated with different (red grey, green, magenta) colours. **c-)** Schematic of cells showing apical contraction (blue arrows), coupled to elongation (red arrows) along the apical axis followed by ingression (green arrow).

Inhibitor studies show that junctional contraction is mediated by non-muscle myosin II in a myosin I dependent manner [3]. We are using various mathematical and modelling techniques to analyse and understand the data. To estimate the forces driving the cell flows we consider the epiblast flows to be analogous to a Stokes flow in a viscous fluid. By solving an inverse problem and assuming a tissue

viscosity we can estimate the distribution and magnitude of the forces driving the tissue flows from the observed velocity fields. We also try to model the individual cell behaviours using a modified active vertex model [4]. Specifically we try to test the hypothesis that junctional myosin accumulation resulting contraction and cell intercalation is a tension sensitive process and that this process can contribute to tissue wide integration of cell behaviours during primitive streak formation.

References

[1] Stern, C.D., *Gastrulation, from cells to embryo's*, ed. C.D. Stern. 2004, New York: Cold Spring Harbor Laboratory Press.

[2] Chuai, M., D. Hughes, and C.J. Weijer, *Collective epithelial and mesenchymal cell migration during gastrulation.* Curr Genomics, 2012. **13**(4): p. 267-77.

[3] Rozbicki, E., et al., *Myosin-II-mediated cell shape changes and cell intercalation contribute to primitive streak formation.* Nat Cell Biol, 2015. **17**(4): p. 397-408.

[4] Barton, D.L., et al., *Active Vertex Model for cell-resolution description of epithelial tissue mechanics.* PLOS Computational Biology, 2017. **13**(6): p. e1005569.

How to model brain tissue?

Alain Goriely

A key problem in the study of the brain is to have reliable models for the response of brain tissues under various stimuli such as mechanical loading, varying pressure, or osmotic variations [5, 6]. In particular, the study of the mechanical response of biological systems within a continuum framework relies on constitutive equations relating stresses to strains [1]. In the absence of a method to derive these constitutive equations from first principles, phenomenological models are routinely used. In particular, when a system behaves in the elastic regime, classes of hyperelastic models have been proposed for many tissues and organs. Ideally, these models are systematically calibrated and validated on multiaxial loading data. Rather than using brute force and fit data to arbitrary strain-energy functions, it is well understood that a key element of constitutive modeling is to consider families of models with desirable properties [9]. For instance, collagen-rich soft tissues are known to be mostly incompressible and display strong strain-stiffening response. Therefore, most of the current models for these tissues start with a functional form that both enforces these particular properties and is general enough to be adapted for specific systems.

However, brain tissue is strikingly different from most soft biological tissues: its microstructure is not governed by collagen and elastin fibers, which implies that brain typically lacks the characteristic strain-stiffening behavior of arteries, skeletal and cardiac muscle, or skin [3, 2]. The typical behavior of these tissues, captured by models such as Fung's or Gent's [4], is that a strong stiffening is obtained at finite extension leading either to a singular limit (in the case of the Gent model) or exponential behavior (for the Fung model). While it is tempting to use such models data analyses shows that these models are not suitable for

brain tissue [8]. Indeed brain tissue is characterized by the following macroscopic properties not found in soft tissues

(i) The shear modulus increases sharply as compression in the direction orthogonal to the shear direction increases;

(ii) The shear modulus remains almost constant or may decrease as tension in the direction orthogonal to the shear direction increases;

(iii) The elastic modulus increases or remains almost constant when compression increases.

A natural problem is then to understand the defining characteristics of brain tissue and to identify a suitable family of hyperelastic models with these characteristics. Moreover, a model for brain tissue needs to be suitable for small to moderate strain as experienced in vivo.
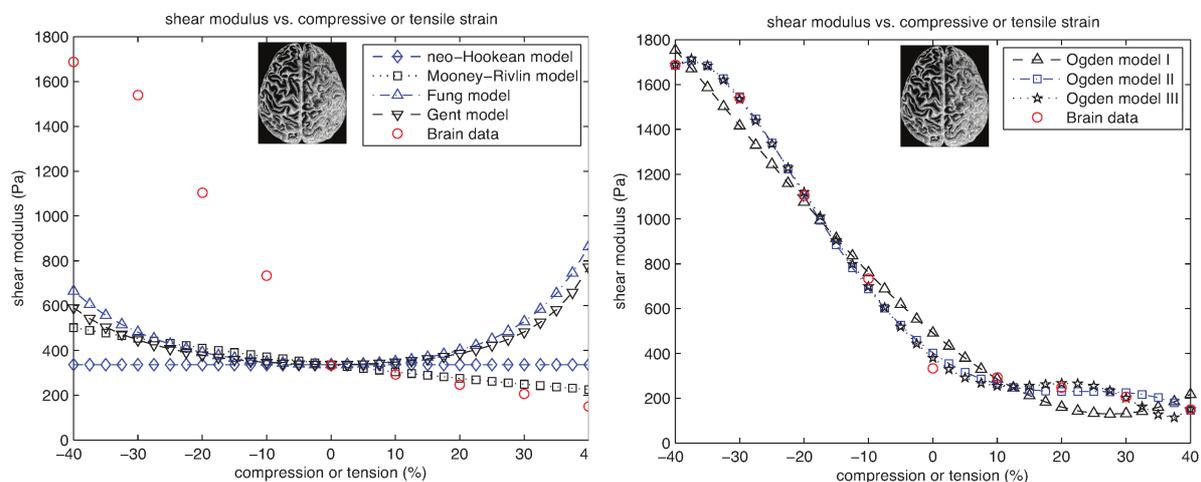
FIGURE 1. Soft-tissue models fail to capture brain tissue stiffening under compression (left) but new phenomenological models (right) capture this behavior [8].

The main mathematical challenge is to build a family of isotropic hyperelastic strain-energy functions, with a small number of parameters, that exhibit this characteristic behavior under combined shear and compression or tension. To achieve this, we have devised a systematic strategy to derive a family of hyperelastic models with a small number of parameters that predict the elastic behavior of brain tissue under combined shear and axial loading and are suitable for finite-element analyses.and demonstrate their performance on experimental data for human brain tissue from [7]. Our algorithmic approach is generic and, as such, applicable to other biological tissues with similar properties, including adipose tissue. The unsuitability of classic soft-tissue models is shown in Fig. 1 together with the new family of models [8].

Yet another fascinating mathematical modeling issue is that biological and synthetic materials often exhibit intrinsic variability in their elastic responses under large strains, owing to microstructural inhomogeneity or when elastic data are

extracted from viscoelastic mechanical tests. For these materials, although hyperelastic models calibrated to mean data are useful, stochastic representations accounting also for data dispersion carry extra information about the variability of material properties found in practical applications. We have combined finite elasticity and information theories to construct homogeneous isotropic hyperelastic models with random field parameters calibrated to discrete mean values and standard deviations of either the stress-strain function or the nonlinear shear modulus, which is a function of the deformation, estimated from experimental tests. These quantities can take on different values, corresponding to possible outcomes of the experiments. As multiple models can be derived that adequately represent the observed phenomena, we have applied Occam's razor by providing an explicit criterion for model selection based on Bayesian statistics. We then employed this criterion to select a model among competing models calibrated to experimental data for brain tissue under single or multiaxial loads [10].

References

[1] GORIELY, A. *The Mathematics and Mechanics of Biological Growth*. Springer Verlag, New York, 2017.

[2] GORIELY, A., BUDDAY, S., AND KUHL, E. Neuromechanics: From Neurons to Brain. *Advances in Applied Mechanics 48* (2015), 79–139.

[3] GORIELY, A., GEERS, M. G. D., HOLZAPFEL, G. A., JAYAMOHAN, J., JÉRUSALEM, A., SIVALOGANATHAN, S., SQUIER, W., VAN DOMMELEN, J. A. W., WATERS, S. L., AND KUHL, E. Mechanics of the brain: perspectives, challenges, and opportunities. *Biomech. Model. Mechanobiol. 14* (2015), 931.

[4] HORGAN, C. O., AND SACCOMANDI, G. A description of arterial wall mechanics using limiting chain extensibility constitutive models. *Biomech. Model. Mechanobiol. 1* (2003).

[5] LANG, G. E., STEWART, P. S., VELLA, D., WATERS, S. L., AND GORIELY, A. Is the Donnan effect sufficient to explain swelling in brain tissue slices? *J. R. Soc. Interface 11*, 96 (2014), 20140123.

[6] LANG, G. E., VELLA, D., WATERS, S. L., AND GORIELY, A. Propagation of damage in brain tissue: Coupling the mechanics of edema and oxygen delivery. *Biomech. Model Mechanobiol. 14* (2015), 1197–1216.

[7] MIHAI, L. A., BUDDAY, S., HOLZAPFEL, G. A., KUHL, E., AND GORIELY, A. A family of hyperelastic models for human brain tissue. *Journal of the Mechanics and Physics of Solids 106* (2017), 60–79.

[8] MIHAI, L. A., CHIN, L., JANMEY, P. A., AND GORIELY, A. A comparison of hyperelastic constitutive models applicable to brain and fat tissues. *J. R. Soc. Interface 12*, 110 (2015), 20150486.

[9] MIHAI, L. A., AND GORIELY, A. How to characterize a nonlinear elastic material? a review on nonlinear constitutive parameters in isotropic finite elasticity. *Proc. R. Soc. A 473*, 2207 (2017), 20170607.

[10] MIHAI, L. A., WOOLLEY, T. E., AND GORIELY, A. Stochastic isotropic hyperelastic materials: constitutive calibration and model selection. *Proc. R. Soc. A 474*, 2211 (2018), 20170858.

Mechanisms of adhesion-independent migration
Dani Bodor

Cell migration is key for many physiological and pathological phenomena, including immune response, wound healing, development and metastasis. Traditionally, cell migration is studied on cultured cells adhering to coverslips, where forces are transmitted onto the surface through integrin-based anchors. However, it has been clearly demonstrated that adhesion is dispensable for efficient migration in vivo and for confined cells. I discuss an alternative migration mode, where confined cells use friction between the actomyosin cortex and the extracellular environment in order to generate traction forces in the absence of any form of adhesion.

Using advanced microfluidics, we could measure the cellular friction coefficient, which allows us to show that friction generates 100-1000-fold lower stresses for efficient migration. By measuring the distance between the cell and the substrate we could show that lubricated friction is insufficient to generate the required force and propose that non-adhesive molecular interactions are required. I also present ongoing efforts to determine which molecules are involved, by combining cell surface mass-spec data with knowledge of extracellular domain size and cortex interactions and testing candidates in microfluidic chips. Ultimately, this will lead to an in depth molecular understanding of a wide-spread yet understudied migration mode.

Multiphase modelling of biological tissue
John King

Multiphase approaches are well suited to the macroscale modelling of a wide variety of biological systems (including tumour growth, tissue engineering, embryo development and bacterial biofilms) due to their capacity to capture multiple cell types, ECM, water, tissue-engineering scaffolds and so on. Here we exemplify how such approaches may play a role in understanding processes such as the contact inhibition of cell division and cell sorting. We limit ourselves to two-phase formulations, though the frameworks readily extend to more.

Firstly, we outline a deriviation of a very simplistic drift-diffusion approach to tissue growth, eschewing any consideration of biomechanics beyond incompressibility of the individual phases. The two phases here are cells (volume fraction n) and water (volume fraction w), with mass conservation implying

$$(1) \qquad \frac{\partial n}{\partial t} + \nabla.(n\mathbf{v}_n) = S(n,w), \ \frac{\partial w}{\partial t} + \nabla.(w\mathbf{v}_w) = -S(n,w),$$

$$(2) \qquad\qquad\qquad\qquad n + w = 1,$$

where S represents cell division or death. We introduce a free energy $\Im$, with density F, that may depend on n, w and on any of their spatial derivatives, say, with

$$(3) \qquad\qquad \Im = \int \left(F[n,w] + p(n+w-1) \right) d\mathbf{x},$$

where p is a Lagrange multiplier enforcing the no voids condition (2). Hence, ignoring any boundary contributions,

$$\frac{d\Im}{dt} = \int \left(\mu_n \frac{\partial n}{\partial t} + \mu_w \frac{\partial w}{\partial t} \right) d\mathbf{x}$$

$$= \int \left(n\mathbf{v}_n.\nabla\mu_n + w\mathbf{v}_w.\nabla\mu_n + (\mu_n - \mu_w)S \right) d\mathbf{x}$$

where

$$\mu_n = \frac{\delta\Im}{\delta n}, \ \mu_w = \frac{\delta\Im}{\delta w}$$

are the relevant chemical potentials and (1) has been used. Next we introduce a Rayleighian dissipation $\Re$ defined by

$$\Re = \int \frac{1}{2} \left(\frac{n}{M_n}|\mathbf{v}_n|^2 + \frac{w}{M_w}|\mathbf{v}_w|^2 \right) d\mathbf{x} + \frac{d\Im}{dt},$$

where M_n and M_w are the respective mobilities, and take the evolution to be governed by the variational derivatives of $\Re$ with respect to $\mathbf{v}_n$ and $\mathbf{v}_w$, treating n and w as if known. We thereby obtain

(4) $$\mathbf{v}_n = -M_n\nabla\mu_n, \ \mathbf{v}_w = -M_w\nabla\mu_w,$$

which could alternatively be prescribed as constitutive assumptions. The energy equation follows from

$$\mathbf{v}_n.\frac{\delta\Re}{\delta\mathbf{v}_n} + \mathbf{v}_w.\frac{\delta\Re}{\delta\mathbf{v}_w} = 0,$$

whereby

$$\frac{\delta\Im}{\delta n}\frac{\delta\mu}{\delta t} + \frac{\delta\Im}{\delta w}\frac{\delta\Im}{\delta t} - \nabla.(n\mu_n\mathbf{v}_n + w\mu_w\mathbf{v}_w) = -\frac{n}{M_n}|\mathbf{v}_n|^2 - \frac{w}{M_w}|\mathbf{v}_w|^2 + (\mu_n - \mu_w)S,$$

wherein the left-hand side is conservative, comprising by Noether's first theorem (associated with invariance under translations of t) $\partial F/\partial t$ and a spatial divergence, and the right-hand side represents the local dissipation, though (unconventionally) S need *not* be chosen to make the phase change contribution $(\mu_n - \mu_w)S$ negative since such models do not attempt to incorporate cellular metabolism (and the process of cell divisions is not reversible). With the standard entropic expression

(5) $$F = kT(n\ln n - n + w\ln w - w)$$

the model in its simplest form reads

$$\frac{\partial n}{\partial t} = \nabla.(D_n\nabla n + M_n \ n\nabla p) + S(n, w), \ \frac{\partial w}{\partial t} = \nabla.(D_w\nabla w + M_w n\nabla p) - S(n, w),$$

$$n + w = 1,$$

D_n, D_w being given by the Einstein relationship $D = kTM$. The simplest assumptions on S are typically

$$S = Kn \text{ or } S = Knw,$$

for constant K, the latter explicitly requiring the presence of water in order to make new cells (and the former should be interpreted as holding only for $w > 0$,

with $S = 0$ for $w = 0$), thereby capturing in a crude fashion aspects of contact inhibition. Stretching the analogy with chemical kinetics might suggest a form such as

$$(6) \qquad\qquad S = K \exp(\mu_n/kT)$$

for S; generalising (5) to

$$F = kT(n \ln n - n + w \ln w - w + \frac{1}{2}\alpha n^2),$$

the α term being intended to capture cell-cell interactions, gives

$$(7) \qquad\qquad \mu_n = kT(\ln n + \alpha n) + p$$

and contact inhibition could then be mimicked via (6) in two distinct ways: $\alpha < 0$ would represent a cell-density-driven mechanism, though $\partial^2 F/\partial n^2 < 0$ would then be possible, leading via (4) to the possibility of backward diffusion (which would require regularisation), while an assumption such as

$$K = K_0 e^{pV/kT}$$

for constants K_0 and (activation volume) V could represent a cell-pressure-driven mechanism so long as (given the p contribution in (7)) the inequality $V > 1$ holds under the current scalings, the interpretation of which is unclear.

The possible presence of backward diffusion hints at a cell-sorting mechanism and our second example involves two cell types, of volume fractions n and m, with (1)-(3) remaining valid with w replaced everywhere by m. In the one-dimensional case (but not in general) we can adopt

$$\Re = \int \frac{1}{2}\kappa|v_n - v_m|^2 dx + \frac{\partial \Im}{\partial t}$$

as the simplest appropriate choice, yielding momentum equations

$$(8) \qquad\qquad 0 = -\frac{\delta\Re}{\delta v_n} = -n\frac{\partial}{\partial x}\mu_n - \kappa(v_n - v_m),$$

$$(9) \qquad\qquad 0 = -\frac{\delta\Re}{\delta v_m} = -m\frac{\partial}{\partial x}\mu_m - \kappa(v_m - v_n),$$

where, because of the two contributions to (3), the derivatives of the chemical potentials contain both Fick (density gradient) and Darcy (pressure gradient) contributions. Overall momentum conservation then follows from summing (8) and (9):

$$(10) \qquad 0 = -\frac{\partial}{\partial x}\left(n\frac{\delta\Im}{\delta n} + m\frac{\delta\Im}{\delta m}\right) + \frac{\delta\Im}{\delta n}\frac{\partial n}{\partial x} + \frac{\delta\Im}{\delta m}\frac{\partial m}{\partial x},$$

the final two terms being an exact spatial derivative, $\partial\Phi/\partial x$ say, due to the invariance of $\Im$ under x tranlations. Inferring

$$nv_n + mv_m = 0$$

from the one-dimensional version of (1), as well as

$$\Phi = n\mu_n + m\mu_m,$$

from (10) then implies

$$v_n = -\frac{nm^2}{\kappa}\frac{\partial}{\partial x}(\mu_n - \mu_m), \ v_m = \frac{n^2m}{\kappa}\frac{\partial}{\partial x}(\mu_n - \mu_m)$$

and hence the formulation reduces to the scalar equation

$$\frac{\partial n}{\partial t} = \frac{\partial}{\partial x}\left(\frac{n^2(1-n)^2}{\kappa(n)}\frac{\partial}{\partial x}(\mu_n - \mu_m)\right) + S(n, 1-n),$$

wherein $S \equiv 0$ is appropriate in the absence of cell differentiation and, under suitable assumptions on F, a Cahn-Hilliard-like model for cell sorting is reproduced, numerous generalisations thereof being of interest.

Acknowledgements

How to shape an Organ? - Computational Models of Organogenesis
DAGMAR IBER
(joint work with the Computational Biology Group (CoBi), ETH Zurich)

Animals develop from a single cell. While much is known about the regulatory programs that control development, it is still an open question how size and shape are determined in a growing animal. The branched trees of lungs, kidneys and many glands provide a fascinating example of complex shape formation. Each organ has its particular shape that enables its function. How is this shape programmed and how is the program executed during development? We combine mathematical modelling with 3D imaging of developing organs to define the mechanisms that guide the branching program in lungs and kidneys.

Here, we consider several distinct aspects: 1) How are branch points defined? 2) How does the epithelium behave? and 3) How is growth terminated?

The emergence of new branches implies a symmetry break. Experiments further demonstrate that the branching programs in lungs and kidneys are highly stereotyped. The Turing mechanism offers an attractive explanation for such reliable symmetry breaks. However, the molecular components of Turing mechanisms are still elusive and the parameter space, for which Turing patterns emerge, is very small for standard Turing models, making it difficult to explain how Turing mechanisms could have evolved. We showed that receptor-ligand interactions of a

specific type can lead to Turing patterns and that the restriction of receptors to single cells results in a huge parameter spaces [3]. The Turing space can be further enlarged by negative feedbacks and by receptor clustering [3]. We showed that branch point selection during lung branching morphogenesis can be explained by both the FGF10-FGFR2b and SHH-PTCH1 interaction, while branch point selection during kidney branching morphogenesis can be explained by the GDNF-RET and FGF10-FGFR2b interaction [6, 5]. The very different branching patterns in lungs and kidneys can thus robustly emerge from the same regulatory mechanism - implemented by very different protein families in the different organs. Using a 3D developmental sequence of lung bud shapes and 2D lung and kidney culture data, we confirmed that only the Turing mechanism but none of the other proposed patterning mechanism can predict the measured embryonic growth fields [4] (Menshykau et al, in revision). Turing mechanisms can yield different patterns for a given parameter set in case of noisy initial conditions. We showed that this limitation can be addressed by expressing the ligand and its receptor in distinct domains. Consistent with this model prediction, co-expression of GDNF and RET in the epithelium results in non-stereotypic branching. Finally, we predicted and confirmed experimentally that the positive feedback between GDNF/RET and WNT11 enables a closer apposition of buds in the kidneys (Menshykau et al., in revision). Ligand-receptor based Turing mechanism are versatile and can therefore, in principle, explain symmetry breaks in many patterning systems, including digit formation in limb development [1].

To simulate signalling on growing cellular domains and to represent the interplay with cell mechanics, we developed the open-source C++ software, `LBIBCell` [7]. The software uses the Lattice Boltzmann (LB) method in combination with an immersed boundary (IB) method to simulate the fluid-structure interaction between fluid and elastic cell boundaries. Signalling can alter the growth rate and mechanical properties of each cell and the tissue properties can affect the signalling. The Iber and the Chopard (Uni Geneva) groups have recently obtained a 4-year SNF Sinergia grant to extend LBIBCell to 3D. The software is currently used in conjunction with microscopy data to explore the mechanisms that enable biased outgrowth of buds during lung and kidney branching morphogenesis and to determine the mechanisms that define epithelial cell organisation.

The packing of cells in epithelia exhibits striking regularities, regardless of the organism and organ. One of these regularities is expressed in Lewis' law, which states that the average apical cell area is linearly related to the number of neighbours, such that cells with larger apical area have on average more neighbours. The driving forces behind the almost 100-year old Lewis' law have remained elusive. We now provide evidence that the observed apical epithelial packing minimizes surface energy. Lewis' law emerges because the apical cell areas then assume the most regular polygonal shapes within a contiguous lattice, thus minimising the average perimeter per cell, and thereby surface energy. Based on our theory, we

predict that the linear Lewis' law generalizes to a quadratic law if the variability in apical areas is increased beyond what is normally found in epithelia. We confirmed this prediction experimentally by generating heterogeneity in cell growth in Drosophila epithelia. Our discovery provides a link between epithelial organisation, cell division, and growth and has implications for the general understanding of epithelial dynamics.

The growth rate of all normal tissues slows down exponentially over time. The underlying mechanism has remained elusive. Growth termination in the *Drosophila* eye disc is the result of cell differentiation. Using data-based modeling, together with the Casares group we defined the core regulatory interactions that control the movement of the differentiation wave in the eye disc, and showed that growth termination requires an independent decline in the growth rate [2]. We further showed that the growth rate in the eye disc declines inversely proportional to the total size of the growing eye disc [9]. The observation is consistent with growth control by dilution of a cytokine, and we showed that the cytokine Unpaired (Upd) presents a suitable candidate for growth control by dilution [8]. Other mechanisms must, however, apply in other organs, as the growth rate in the *Drosophila* wing disc is not controlled by dilution [10].

In conclusion, data-based modelling can be used to define mechanisms for fundamental developmental processes such as the control of branching morphogenesis, the organisation of epithelia, and growth control.

References

[1] A Badugu, C. Kraemer, Ph. Germann, D. Menshykau, and D. Iber. Digit patterning during limb development as a result of the bmp-receptor interaction. *Scientific Reports*, 2:991, 2012.

[2] P. Fried, M. Sanchez-Aragon, D. Aguilar-Hidalgo, B. Lehtinen, F. Casares, and D. Iber. A model of the spatio-temporal dynamics of drosophila eye disc development. *PLoS Comput Biol*, 12(9):e1005052, 2016.

[3] Tamás Kurics, Denis Menshykau, and Dagmar Iber. Feedback, receptor clustering, and receptor restriction to single cells yield large turing spaces for ligand-receptor-based turing models. *Phys. Rev. E*, 90:022716, Aug 2014.

[4] D. Menshykau, P. Blanc, E. Unal, S Vincent, and D. Iber. An interplay of geometry and signaling enables robust branching morphogenesis. *Development*, 141:4526–4536, 2014.

[5] D Menshykau and D Iber. Kidney branching morphogenesis under the control of a ligand-receptor based turing mechanism. *Phys Biol*, 10:046003, 2013.

[6] D Menshykau, C Kraemer, and D Iber. Branch Mode Selection during early Lung Development. *PLoS Comp Biol*, 8(2):e1002377, 2012.

[7] Simon Tanaka, David Sichau, and Dagmar Iber. Lbibcell: A cell-based simulation environment for morphogenetic problems. *Bioinformatics*, 2015.

[8] J. Vollmer, P. Fried, D. Aguilar-Hidalgo, M. Sanchez-Aragon, A. Iannini, F. Casares, and D. Iber. Growth control in the drosophila eye disc by the cytokine unpaired. *Development*, 144(5):837–843, 2017.

[9] J. Vollmer, P. Fried, M. Sanchez-Aragon, C. S. Lopes, F. Casares, and D. Iber. A quantitative analysis of growth control in the drosophila eye disc. *Development*, 143(9):1482–90, 2016.

[10] J. Vollmer and D. Iber. An unbiased analysis of candidate mechanisms for the regulation of drosophila wing disc growth. *Sci Rep*, 6:39228, 2016.

Indentation of spherical shells: Bistability and Buckling

Matteo Taffetani

(joint work with Dominic Vella)

Simple biological structures like cells and viruses can be modelled as shell structures that enclose a low pressurized environment or a soft substrate. Interesting mathematical questions are related to the understanding of how they interact with the surrounding environment, in term of their response to external stimuli or their locomotion. Indeed, indentation of a spherical structure can be used to probe its mechanical properties [1] while buckling and snap-through instability in shell have been proved to be an effective way to generate motion in microswimmers [2]; moreover, superficial wrinkling induced by indentation can be used to modify the properties of a shell with a potential application toward its functionalization.

The general idea behind this work is to show novel evidences on the bistability and buckling of spherical shells and to provide mathematical explanations of these phenomena. A known result of calculus of variation states that a non-trivial configuration accommodated by a poked elastic spherical shell subjected to large displacements can be represented as an isometric transformation described by a local eversion, i.e. an axisymmetric 'mirror buckled' shape [3]. This deformed solution is energetically favourable since the work due to the indentation is mainly concentrated into the circular ridge that connects the region where the spherical cap is everted to the region where the shell remains undeformed: the energy of this solution vanishes as $\sim h^{5/2}$ with a decreasing thickness h.

Here the attention is posed on two interesting questions on the behaviour of spherical shells *beyond* the axisymmetric 'mirror buckled' shape. (i) The existence of a stable axisymmetric configuration (other than the natural one) of the inverted shell without the application of any point force, i.e. a self-equilibrated 'mirror everted' shape analogous to the 'mirror buckled' shape but with the plane of reflection coincident with the plane of the planform of the shell, and the robustness of this everted configuration against a singular perturbation represented by a force indentation. (ii) If a shell in its natural configuration is indented at its apex, the mirror buckling is unlikely to be observed, since indentation drives to either wrinkling (in pressurized shell) or polygonal buckling (in pressureless shell). In the former case it can be shown analytically that the nonlinear wrinkling features in the limit of large pressurization and large displacement are mainly governed by geometric effects due to a combination between the natural curvature and the curvature induced by the indentations, thus defining a different type of isometry known as 'asymptotic wrinkly isometry' [4].

Limiting to the case of axisymmetric solutions, a pressureless spherical shell is monostabile if the only self-equilibrated state is the natural configuration while it is bistabile if also the stable axisymmetric 'mirror everted' configuration exists. A

deep shell can be described in term of three dimensionless parameters: the Poisson ratio ν; a term related to the depth of the shell, as its solid angle α; a term that describes the balance between the stretching and the bending energies, thus depending on the shell thickness λ. By making use of finite element simulations, the monostability/bistability threshold can be been identified up to almost a complete hemisphere. While remaining within a small error, the same threshold can be computed through a continuation analysis based on the shallow shell equations: then, we can employ the shallow shell limit to compute the monostable/bistable threshold that, in term of λ, does not depend on α and varies linearly against ν: $\lambda_{th} \approx 1.44\nu + 5.06$. A natural way to connect these two self-equilibrated states (while in the bistable parameters regime) is through pointwise indentation. Although the existence of both these two self-equilibrated states, it is possible to show that a shell can asymmetric buckle before the snap-through point is reached. Employing the shallow shell theory, the comparison between indentation from natural and indentation from 'mirror eversion' reveals that: (i) very thin shell always prefers to buckle before the snapping occurs with the marginal stable mode of the polygonal buckling that depends on the type of conditions applied along the external boundary; if the boundary is free to deform in-plane, the polygonal buckling with mode 2 is observed while mode 3 is approached when the thickness is decreased. (ii) Thicker shells always admit a axisymmetric path that continuosly connects the two stable solutions. (iii) In between these two limits, there exist a regime where the snap-through process becomes asymmetric. This work also provides new insights on the robustness of the 'mirror buckling' symmetry of spherical shell caps: indeed, although indentation leads to asymmetrical buckling before snap-through for thin shells, they are also more 'robust' to snap-through.

In the domain where the indentation of a spherical shell induces buckling, the second question is related to the evolution of this asymmetric pattern well beyond the linear threshold: the circumferential axisymmetric ridge eventually becomes linearly unstable in favour of (i) a wrinkled pattern in pressurized shells and (ii) a polygonal buckled shape in pressureless shells. In the former case, finite element evidences show that the circumferential wavenumber m of the wrinkling pattern in the far from threshold regime varies -increases, more specifically- with the distance from the point of indentation and with the indentation applied itself. A asymptotic expansion of the equilibrium and constitutive equations in the small parameter $(1/m)$ shows that the wrinkled pattern arises to relieve the excess in the hoop compression, consistently with what expected in the tension field theory [5], and allows to derive theoretical correlations that relate the spatial variation of m to the mechanical and geometrical properties of the shell: m depends on the *local* (i.e. function of the spatial position r) balance between bending and stretching energies, with the latter mainly due to the competition between the natural curvature of the shell and the one induced by the indentation along the wrinkles. Interestingly, in the largest part of the wrinkled domain the wavenumber depends only on the geometrical parameter of the problem as $m \sim \left(\delta/h\right)^{1/2} \left(r/\sqrt{\delta R}\right)^{3/2}$,

with R and th the undeformed radius and the thickness of the shell and δ the applied displacement of the apex. More challenging is the case of indentation of pressureless spherical shells. Evidences from finite element simulations show that buckling is initially of polygonal and, possibly, it is followed by a crumpled state for very large indentations. In this regime, a clear description of he buckled pattern in the far from threshold limit has still not been proposed.

The proposed approach can be extended to the mechanical/mathematical investigation of similar configurations, i.e. a shell over a different types of substrate, but with asymmetric initial geometries. The case of a substrate with vanishing properties remains unclear and its explanation is still an open interesting problem: in this case, the lack of a characteristic length due to the balance between the elasticity of the shell and the properties of the substrate can induce localization as a response of a compressive loading. Initially this localization induced by the indentation emerges as the formation of a circular ridge that eventually buckles. The open question is then to understand why this happens and how it evolves.

REFERENCES

[1] D. Vella, A. Ajdari, A. Vaziri, A. Boudaoud *The indentation of pressurized elastic shells: from polymeric capsules to yeast cells*, Journal of the Royal Society Interface **9** (2012), 448–455
[2] A. Djellouli, P. Marmottant, H. Djeridi, C. Quilliet, G. Coupier *Buckling instability causes inertial thrust for spherical swimmers at all scales*, Physical Review Letters **119** (2017), 224501:1–5
[3] A.V. Pogorelov, *Bending of surfaces and stability of shells*, AMS Bookstore **72** (1988).
[4] D. Vella, H. Ebrahimi, A. Vaziri, B. Davidovitch, *Wrinkling reveals a new isometry of pressurized elastic shells*, Europhysics Letters **112**, 24007:1–6
[5] A.C. Pipkin, *The relaxed energy density for isotropic elastic memebrane*, Journal of Applied Mathematics **36** (1986) ,85–99.

Forces in Biosystems

REINHARD LIPOWSKY

The bottom-up approach to synthetic biology requires a detailed understanding of the basic construction modules that are necessary for their controlled assembly and integration into artificial protocells. These modules include membrane compartments as provided by giant vesicles, biomolecular machines such as cytoskeletal motors and filaments as well as template-controlled assemblers such as ribosomes. These modules experience intermolecular forces with each other and with their aqueous environments, respond to externally applied forces, and generate local forces when coupled to exergonic chemical reactions such as ATP hydrolysis.

Giant vesicles provide a direct connection between the nano- and the microregime. Indeed, these vesicles represent cell-like compartments with linear dimensions of many micrometers but are enclosed by single molecular bilayers that have a thickness of a few nanometers. The bilayer membranes respond sensitively to molecular

interactions with solutes, biopolymers, and nanoparticles. These nanoscopic responses are amplified by the giant vesicles and can then be studied on much larger scales by optical microscopy. When the membranes are exposed to an asymmetric environment, they acquire a spontaneous curvature and tend to form membrane nanotubes. [1] Several quantitative methods have been recently developed by which one can deduce the value of the spontaneous curvature and of the associated spontaneous tension from the morphology of the tubulated vesicles. [2, 3, 4] In addition, it has been demonstrated by micropipette aspiration and changes in the osmotic conditions that the membrane nanotubes increase the robustness of giant vesicles to mechanical perturbations, [3].

The interactions of nanoparticles with biomembranes are essential for many processes such as biomedical imaging, drug delivery, nanotoxicity, and viral infection. In order to enter the cell, the particle must cross the cell membrane via endocytosis, a process that consists of three substeps: adhesion of the nanoparticle to the membrane; complete engulfment of this particle by the membrane, which then forms a narrow membrane neck that connects the particle-bound membrane segment to the mother vesicle; and cleavage or scission of the membrane neck. All three substeps are governed by the interplay between curvature elasticity and membrane-particle adhesion and can be understood in terms of a few key parameters: particle size, adhesive strength of membrane-particle interactions, as well as bending rigidity and spontaneous curvature of the membrane. The onset of adhesion is described by an instability condition that depends on particle size, adhesive strength, and bending rigidity. [5] The complete engulfment is governed by a stability condition that involves the spontaneous curvature as well. [5, 6] Finally, the scission of the membrane neck can be understood in terms of effective constriction forces which are generated by the spontaneous curvature or by the adhesive nanoparticle. [6] The underlying theory has been extended to Janus particles, which experience curvature-induced forces that push the particles towards local minima of membrane curvature [7], and to the adhesion-induced fission of membranes by ESCRT proteins, for which a minimal system based on giant vesicles and only three proteins has been recently established [8].

Another relatively new research area are giant vesicles exposed to aqueous two-phase systems and water-in-water emulsions. [9, 10] These systems exhibit a variety of wetting morphologies and morphological transformations that reflect both the capillary forces arising from the water-water interfaces and the membrane curvature generated by the asymmetric aqueous environments. Striking wetting morphologies have also been observed for the recently discovered membraneless organelles that behave like liquid droplets. [11]

At the end, a brief outlook was given on cooperative transport by teams of molecular motors [12, 13], on protein synthesis by ribosomes [14], and on the perspectives arising from the sequential bottom-up assembly of synthetic cells that has been achieved very recently using microfluidic emulsion droplets [15].

REFERENCES

[1] R. Lipowsky. *Faraday Discuss.* 161, 305 (2013)
[2] Y. Liu, J et al. *ACS Nano* 10, 463 (2016)
[3] T. Bhatia et al. *ACS Nano*, DOI: 10.1021/acsnano.8b00640 (in press)
[4] R. Dasgupta et al, *PNAS*, DOI: 10.1073/pnas.1722320115 (in press)
[5] J. Agudo-Canalejo and R. Lipowsky. *ACS Nano* 9, 3704 (2015); and *Nano Letters* 15, 7168 (2015)
[6] J. Agudo-Canalejo and R. Lipowsky. *Soft Matter* 12, 8155 (2016)
[7] J. Agudo-Canalejo and R. Lipowsky. *Soft Matter* 13, 2155 (2017)
[8] Y. Avalos-Padilla et al. *Front. Cell. Infect. Microbiol.* 8:53 (2018)
[9] Y. Li, R. Lipowsky, and R. Dimova. *JACS* 130, 12252 (2008)
[10] R. Lipowsky, *J. Chem. Phys. B* 122, 3572 (2018)
[11] R. Knorr, T. Franzmann, A. Hyman, R. Dimova, and R. Lipowsky, in preparation.
[12] M. Müller, S. Klumpp, and R. Lipowsky. *PNAS* 105, 4609 (2008)
[13] M. Ucar and R. Lipowsky. *Soft Matter* 13, 328 (2017)
[14] S. Rudorf and R. Lipowsky, *PLoS ONE* 10, e013494 (2015)
[15] M. Weiss et al. *Nature Materials* 17, 89 (2018)

Mechanotransduction by engineered extracellular matrices

BRITTA TRAPPMANN

Cell fate decisions are influenced by many cues, which together constitute the cell microenvironment. One critical regulator is the extracellular matrix (ECM), which varies not only in composition, but also in physical properties such as stiffness. The impact of matrix stiffness on cell spreading and differentiation has been studied intensively on 2D surfaces using synthetic hydrogels, but very little is known about stiffness sensing within more complex 3D matrices.

Unlike linear elastic hydrogels, most natural tissues are fibrous. To investigate how cells sense stiffness in settings structurally similar to native ECMs, we designed a synthetic fibrous material with tunable mechanics. Increasing fiber stiffness suppressed mesenchymal stem cell spreading and proliferation, in contrast to flat hydrogels. We identified fiber recruitment as a mechanism by which cells actively probe and respond to the mechanics of fibrous environments.

Furthermore, a hurdle in 3D contexts is to isolate the role of ECM stiffness from other matrix properties, in particular degradability. If cells are fully encapsulated, changes in bulk stiffness also influence the amount of matrix crosslinks that a cell has to cleave in order to spread and interact with its surroundings, impacting cell shape and function. Here, we have developed a sugar-based hydrogel system that offers independent control over mechanical properties, adhesive ligand density and matrix degradation rates. The material can be processed under physiologic conditions rendering it suitable for cell encapsulation. Matrix metalloproteinase (MMP)

cleavable peptides as crosslinking units enable cellular matrix remodeling and variation of their sequence gives access to a range of degradation rates. Using this system, we study the impact of matrix stiffness and degradability on angiogenic sprouting. In particular, we demonstrate that matrix degradability and mechanics control the multicellularity of 3D endothelial cell invasion.

<div align="center">REFERENCES</div>

[1] *Matrix degradability controls multicellularity of 3D cell migration.* B. Trappmann, B. M. Baker, W. J. Polacheck, C. K. Choi, J. A. Burdick, C. S. Chen, Nat. Commun. 2017, 8, 371.

[2] *Cell-mediated fiber recruitment drives extracellular matrix mechanosensing in engineered fibrillar microenvironments.* B. M. Baker, B. Trappmann, W. Y. Wang, M. S. Sakar, I. L. Kim, V. B. Shenoy, J. A. Burdick, C. S. Chen, Nat. Mater. 2015, 14, 1262-1268.

[3] *How cells sense extracellular matrix stiffness: a material's perspective.* B. Trappmann, C. S. Chen, Curr. Opin. Biotech. 2013, 24, 948-953.

Symmetry breaking and self-organisation in mouse development

<div align="center">Takashi Hiiragi</div>

<div align="center">(joint work with Dimitri Fabrèges)</div>

A defining feature of living systems is the capacity to break symmetry and generate well-defined forms and patterns through self-organisation. Our group aims to understand the principle of multi-cellular self-organisation using a well-suited model system: early mouse embryos. Mammalian eggs lack polarity and thus symmetry is broken during early embryogenesis. This symmetry breaking results in the formation of a blastocyst consisting of two major cell types, the inner cell mass and the trophectoderm, each distinct in its position and gene expression. Our recent studies unexpectedly revealed that morphogenesis and gene expression are highly dynamic and stochastically variable during this process (Dietrich et al. 2015; Ohnishi et al. 2014). Determining which signal breaks the symmetry and how the blastocyst establishes a reproducible shape and pattern despite the preceding variability remains fundamental open questions in mammalian development. We have recently developed a unique set of experimental frameworks that integrate biology, physics and mathematical modelling. Using a reduced system, we find that Cdh1-independent contact asymmetry directs temporally-controlled apical domain formation, which is necessary and sufficient for symmetry breaking and segregating the first cell lineages in mouse development (Korotkevich et al. 2017). Furthermore, we show that asymmetric segregation of the apical domain generates blastomeres with different contractility, which triggers their sorting into inner and outer positions (Maître et al. 2015; Maître et al. 2016). Hence, contractility couples the positioning and fate specification of blastomeres, and this mechanism ensures the robust self-organization of the blastocyst and confers remarkable regulative capacities to early mammalian embryos. We aim to understand how molecular, cellular and physical signals are dynamically coupled across the scales for self-organisation during early mammalian development.

References

[1] Dietrich, J.-E., Panavaite, L., Gunther, S., Wennekamp, S., Groner, A.C., Pigge, A., Salven-moser, S., Trono, D., Hufnagel, L. and Hiiragi, T.: *Venus trap in the mouse embryo reveals distinct molecular dynamics underlying specification of first embryonic lineages.* EMBO reports (2015) 16(8), 1005-1021.

[2] Korotkevich, E., Niwayama, R., Courtois, A., Friese, S., Berger, N., Buchholz, F. and Hiiragi, T.: *The Apical Domain Is Required and Sufficient for the First Lineage Segregation in the Mouse Embryo.* Developmental Cell (2017) 40(3), 235–247.e7.

[3] Maître, J.-L., Niwayama, R., Turlier, H., Nédélec, F. and Hiiragi, T.: *Pulsatile cell-autonomous contractility drives compaction in the mouse embryo.* Nat Cell Biol (2015) 17, 849–855.

[4] Maître, J.-L., Turlier, H., Illukkumbura, R., Eismann, B., Niwayama, R., Nedelec, F. and Hiiragi, T.: *Asymmetric division of contractile domains couples cell positioning and fate specification.* Nature (2016) 536(7616), 344–348.

[5] Ohnishi, Y., Huber, W., Tsumura, A., Kang, M., Xenopoulos, P., Kurimoto, K., Oleś, A.K., Araúzo-Bravo, M.J., Saitou, M., Hadjantonakis, A.-K. and Hiiragi, T.: *Cell-to-cell expression variability followed by signal reinforcement progressively segregates early mouse lineages.* Nat Cell Biol (2014) 16, 27–37.

Modeling large-scale cell migration and proliferation with mechanical and biochemical interactions: Bridging discrete and continuum via dynamic cellular finite-element method (DyCelFEM) method and Accurate Chemical Master Equation solutions

Jie Liang

(joint work with Youfang Cao, Jieling Zhao, Anna Terebus, Margaret Gardel, Luisa DiPietro)

A challenging task in cell and tissue modeling is to account for changes in cellular shapes, topological arrangement, and physical mechanics across the scale when there are a thousands of migrating and interacting cells. In addition, the reconciliation of the discrete nature of individual cells and the continuum mechanical description of tissues remains a difficult task. Furthermore, integrating cellular mechanics with biochemical signaling networks controlling cellular behavior poses an additional challenge.

We have been developing a method, called the dynamic cellular finite-element model (DyCelFEM), to bridge these gaps [1]. Our approach accounts for changes in cellular topology, cellular shapes, and cellular mechanics, and models the full range of cell motion, from movements of individual cells to collective cell migrations. The transmission of mechanical forces regulated by intercellular adhesions and their ruptures are also accounted for. Intra-cellular protein signaling networks controlling cell behaviors are also embedded in individual cells. With this approach, we can examine specific effects of biochemical and mechanical cues in regulating cell migration and proliferation, and in controlling tissue patterning. Using a simplified re-epithelialization model of wound tissue, our simulation results using DyCelFEM suggest that biochemical cues are better at guiding cell migration with improved directionality and persistence, while mechanical cues are

better at coordinating collective cell migration. We also discuss an example using DyCelFEM to study the movement of a single cell interacting with ECM-like medium. Please see [1] for more details.

As molecular interaction network control cellular behavior, and often such mesocopic networks are stochastic in nature, the discrete Chemical Master Equation (dCME) provides a fundamental framework to study a large class of stochastic networks that underly diverse biological phenomena. These include stem cell differentiatoin, cellular fate decision, and tumorogenesis. There are a number of challenges when solving dCMEs arising from stochastic networks: How do we know if the computed peaks of probability mass are complete and we are not missing anything important? How to be sure if the computed probability landscape is not erroneous? How to accurately compute probabilities of rare events (e.g., 10^{-12})? What are the best accuracy we can hope to achieve with a laptop, or with a giant computer? Answers to these important question are largely unknown except for a few simple toy examples. Overall, we cannot distinguish if a network model is incorrect or the computational solution is inadequate.

In this talk, we discussed how these important questions can be answered for a large class of stochastic networks using the n-simplex optimal state enumeration algorithm and the ACME (accurate chemical master equation) method [2, 3]. We discuss how exact time-evolving probabilistic landscapes can be computed without Monte Carlo simulation or Fokker-Planck/Langevin approximation. In addition, we discuss how a priori error bound of the steady state probability landscape due to state space truncation that is inevitable for complex networks can be constructed, without trial simulation using the quotient matrix technique. We revisit details of dynamics of probability landscapes of a number of stochastic networks, and give examples on how exact results can be computed for large stochastic network (16-nodes), and how to relate the computed probability landscape to phenomenological characterization of cellular decision networks such as bi-stability, epigenetic states, and the robustness of wild type versus mutants. Recent development in theory of discrete probability flux and velocity are also be discussed. Biological examples of solving the puzzles of phage lambda and HIV latency are briefly be discussed. (Please see [3] and [2] and `gila.bioe.uic.edu/liang/liang\_pub.html` for further information).

<div align="center">REFERENCES</div>

[1] Jieling Zhao, Youfang Cao, Luisa DiPietro, and Jie Liang. *Dynamic cellular finite element method for modeling large scale cell migration and proliferation under the control of mechanical and biochemical cues: A study of re-epithelialization.* Journal of the Royal Society Interface, **14**:20160959, 2017, `http://dx.doi.org/10.1098/rsif.2016.0959`

[2] Youfang Cao, Anna Terebus, and Jie Liang. *State space truncation with quantified errors for accurate solutions to discrete Chemical Master Equation.* Bulletin of Mathematical Biology, **78**(4):617–661, 2016. PMCID: PMC4896403, `https://doi.org/10.1007/s11538-016-0149-1`

[3] Youfang Cao, Anna Terebus, and Jie Liang. *Accurate Chemical Master Equation solution using multi-finite buffers.* SIAM Multiscale Modeling and Simulation. **14**(2):923–963, 2016. PMCID: PMC4896403, `https://doi.org/10.1137/15M1034180`

Life is Different: it is Inherited
Bob Eisenberg

What is different about life? Why do life sciences require different science and mathematics? I address these issues starting from the obvious: all of life is inherited from genes. Twenty thousand genes of say 30 atoms each control an animal of ~ 1025 atoms. How is that possible? Answer: the structures of life form a hierarchy of devices that allow handfuls of atoms to control everything. A nerve signal involves meters of nerve but is controlled by a few atoms. Indeed, potassium and sodium differ only in the diameter of the atoms. Life depends on this difference in diameter. Sodium and potassium are otherwise identical. The task of the biological scientist is first to identify the hierarchy of devices and what they do. Then we want to know how the devices work. We want to understand life well enough to improve its devices, in disease and technology.

Patterning through growth
Arnd Scheel

Pattern formation has been studied extensively, mostly in the context of linear instabilities and the selection of wavenumbers through linear dispersion relations. One starts from the idea that a physical systems is quenched, such that a trivial state looses stability. Random, or white noise small amplitude perturbations then induce exponential growth of certain Fourier modes. This talk focuses on two aspects of this pattern formation scenario. First, the selection of finite Fourier wavenumbers and thereby of patterns with a distinguished wavelength usually requires rather complex mechanisms, such as disparate rates of diffusivity as suggested in Turing's seminal work. Second, random initial conditions typically lead to highly disorganized patterns with many defects, that may or may not evolve towards a simpler crystalline structure.

The first part of the talk shows how very simple systems may exhibit pattern formation with selected, well-defined wavenumbers, when initial conditions are *shot noise* perturbations of a quenched, unstable state. A first example is the reaction-diffusion system

$$c_t = \Delta c - f(c, e)$$
$$e_t = \kappa \Delta e + f(c, e),$$

with cubic nonlinearity $f(c, e) = e(1 - e)(e - a) + \gamma c$, $0 < a < 1$, $\gamma > 0$. Linear instabilities of $e \equiv a$, $c \equiv 0$ do *not* select finite wavenumbers. Most dramatically, in the case $\kappa = 0$, white noise perturbations of this state lead to highly disorganized patterns on arbitrarily fine length scales, not subject to coarsening. On the other hand, shot noise perturbations generate regular periodic patterns with finite wavelength [6]. The talk briefly reviews methods that allow to predict these wavenumbers [10] and presents extensions to run-and-tumble systems [11]. In a

related direction, deposition of mass through a source term $h(\xi)$ with finite mass $\int h < \infty$,

$$c_t = \Delta c - f(c, e) + ch(x - ct)$$
$$e_t = \kappa \Delta e + f(c, e),$$

and stable initial conditions $e \equiv c \equiv 0$, can also lead to regular patterns in the wake of the deposition front propagating at speed c.

The second part of the talk studies this directional quenching procedure in more detail. It turns out that the growth process can effectively select patterns and avoid defect formation, thus leading to pure crystalline patterns in its wake. We study systems where a trivial state is unstable in a growing subset Ω_t of the plane. Examples are the Allen-Cahn equation,

$$u_t = \Delta u - \mu \mathrm{sign}(x - ct)u - u^3,$$

the Cahn-Hilliard equation,

$$u_t = -\Delta \left(\Delta u - \mu \mathrm{sign}(x - ct)u - u^3 \right),$$

and the Swift-Hohenberg equation,

$$u_t = -\left(1 + \Delta\right)^2 u - \mu \mathrm{sign}(x - ct)u - u^3,$$

with parameter jump at the boundary of Ω_t, chosen for instance as $\{x < ct\}$. One is then interested in the emergence of striped patterns in Ω_t, and how they are selected by the growth mechanism, that is, by the geometry of Ω_t. Phenomenologically, one notices that stripes are perpendicular to the boundary of Ω_t in the Allen-Cahn equation. In both Cahn-Hilliard and Swift-Hohenberg equation, stripes are parallel to the boundary for large rates of growth, but tend to be perpendicular for slow growth. We present theoretical results that explain this dichotomy and predict alignment and strain in striped phases arising through growth [1, 2, 3, 4, 5, 7, 8, 9, 10, 12]. The key object is a moduli space $\mathcal{M} \subset \mathbf{R}^3$, which contains points (k_x, k_y, c) corresponding to pure crystalline growth at rate c, creating striped patterns with wave vector $\underline{k} = (k_x, k_y)$. More precisely, we consider $\Omega_t = \{x < ct\}$ and look for "simplest" solutions to the underlying equations that leave behind striped patterns with wave vector $\underline{k}$ that is, solutions that converge to periodic patterns $u_\mathrm{p}(k_x x + k_y y; k)$, $u_\mathrm{p}(\xi; k) = u_\mathrm{p}(\xi + 2\pi; k)$, $k = |\underline{k}|$, as $x \to -\infty$, and that are periodic or stationary in appropriately comoving frames. In the case of the Allen-Cahn equation, the moduli space is completely characterized as a quarter of an ellipse in the $k_x = 0$ plane, and a line segment in $c = k_y = 0$. The moduli space in Swift-Hohenberg is similarly described as a surface over such a quarter ellipse, together with a line segment in $k_y = c = 0$, but contains a number of interesting singularities near boundaries.

In conclusion, we relate these moduli spaces to observations in direct simulations, and point to a number of open problems and future directions.

REFERENCES

[1] R. Goh, R. Beekie, D. Matthias, J. Nunley, & A.Scheel *Universal wavenumber selection laws in apical growth.* Phys. Rev. E, **94** (2016), 022219.

[2] R. Goh & A. Scheel. *Triggered fronts in the complex Ginzburg Landau equation.* J. Nonlinear Science **24** (2014), 117–144.

[3] R. Goh & A. Scheel. *Hopf bifurcation from fronts in the Cahn-Hilliard equation.* Arch. Rat. Mech. Anal. 217 (2015), 1219-1263.

[4] R. Goh & A. Scheel. *Pattern formation in the wake of triggered pushed fronts.* Nonlinearity **29** (2016), 2196–2237.

[5] R. Goh & A. Scheel. *Pattern-forming fronts in a Swift-Hohenberg equation with directional quenching — parallel and oblique stripes.* J. London Math. Soc., to appear.

[6] M. Kotzagiannidis, J. Peterson, J. Redford, A. Scheel & Q. Wu. *1Stable pattern selection through invasion fronts in closed two-species reaction-diffusion systems.* In RIMS Kôkyûroku Bessatsu **B31** (2012), Far-From-Equilibrium Dynamics, eds. T. Ogawa, K. Ueda, pp 79–93.

[7] R. Monteiro & A. Scheel. *Phase separation patterns from directional quenching.* J. Nonl. Sci. **27** (2017), 1339–1378.

[8] R. Monteiro & A. Scheel. *Contact angle selection for interfaces in growing domains.* ZAMM, to appear.

[9] D. Morrissey & A. Scheel. *Characterizing the effect of boundary conditions on striped phases.* SIAM J. Appl. Dyn. Syst. **14** (2015), 1387–1417.

[10] A. Scheel & M. Holzer. *Criteria for pointwise growth and their role in invasion processes.* J. Nonl. Sci. **24** (2014), 661–709.

[11] A. Scheel & A. Stevens. *Wavenumber selection in coupled transport equations.* J. Math. Biol. **75** (2017), 1047–1073.

[12] A. Scheel & J. Weinburd. *Wavenumber selection via spatial parameter jump.* Phil. Trans. Roy. Soc. A, **376** (2017), 20170191.

Tissue self-organization through mechanical feedback

PIERRE DEGOND

(joint work with Diane Peurichard, Fanny Delebecque, Anne Lorsignol, Corinne Barreau, Jacques Rouquette, Xavier Descombes, Louis Casteilla)

In this talk, we mostly report on the work published in [1] about self-organization of adipose tissue. Adipose tissue is constituted of clusters of fat cells (adipocytes) named lobules separated by walls composed of extracellular matrix (ECM). During development, they emerge from an unstructured fiber network containing cells.

In the present work, we show that directionally organized cell and fiber structures can emerge as a result of simple mechanical interactions between the cells and the fiber network. We consider a two-dimensional microscopic model to test a scenario in which the mutual repulsion between cells modelled as non-deformable and non-overlapping spheres and ECM elements modelled as segments having the ability of cross-linking to each other shape the organization of the tissue.

The results of the model are compared with biological data acquired on fixed mouse adipose tissue which has been immuno-stained for segmentation of cell and lobule boundaries. The model shows that two parameters play a key role: the proportion of linked fiber pairs (which is related to the stiffness of the ECM) and

the fiber unlinking frequency (related to the ECM plasticity). We outline three zones of this two-dimensional parameter space separated by abrupt transition regions which can be associated with healthy or pathological tissues respectively. We also provide parameter conditions that allow us to recover the observed biological tissues.

We have also presented results of ongoing work which use the present work to explore the conditions for healing or regeneration of injured tissues.

REFERENCES

[1] D. Peurichard, F. Delebecque, A. Lorsignol, C. Barreau, J. Rouquette, X. Descombes, L. Casteilla, P. Degond, *Simple mechanical cues could explain adipose tissue morphology*, J. Theoret. Biol., **429** (2017), 61–81.

Chemical potential rather than concentration should be used to characterize plasma membrane cholesterol

FREDRIC S. COHEN

(joint work with Artem G. Ayuyan)

The importance of cholesterol is appreciated by the public and scientists alike. The cholesterol content in blood plasma of individuals is routinely clinically measured. Despite the importance of blood cholesterol, the overwhelming majority of cholesterol, $\sim 90\%$, resides in cells, and of this 90%, $\sim 80\%$ is within plasma membranes. Cholesterol constitutes, on a mole basis, more than $1/3$ of plasma membrane lipid molecules. At such a high density, it is a priori likely that cholesterol's interactions would have profound effects on biological processes, yet cholesterol is routinely characterized by its concentration, rather than by its chemical activity.

In the absence of interactions, the chemical potential of a substance, μ, is given by $\mu = \mu_0 + k_B T \ln C$, where μ_0 is a standard chemical potential (reference energy), C is the concentration of the substance, and k_B and T have their usual meaning. Interactions can be readily accounted for through the equation $\mu = \mu_0 + k_B T \ln C + \text{energy of interactions}$. This equation yields the free energy per molecule and is often written as $\mu = \mu_0 + k_B T \ln a$, where a is chemical activity. The term a incorporates the energy of interactions, allowing the chemical potential to be written in similar forms in the absence of interactions (an ideal solution), and in the presence of interactions (a real solution).

We have developed a way to experimentally measure the chemical potential of cholesterol in plasma membranes of cells, μ_{CH}. The logical basis of the method rests on a fundamental consequence of the definition of chemical potential: molecules move from high to low chemical potential between two media; movement ceases only when the chemical potential of a substance is equal in the two media – the substance is at equilibrium. Using this fundamental principle, we reasoned that if a water-soluble carrier of cholesterol was included in the extracellular solution bathing cells, cholesterol would move between the aqueous solution and the cell membrane until their cholesterol chemical potentials equalized. Cholesterol

concentration is readily measured (as blood cholesterol is measured) and so, if the cholesterol concentration in the carrier-containing aqueous phase could be related to chemical potential, the cholesterol chemical potential of the plasma membranes, μ_{CH}, would also be known. We obtained this relationship by noting that if an ideal solution were brought into contact with a non-ideal aqueous solution that contains cholesterol and a carrier for it, the chemical potential of the non-ideal solution will equilibrate to that of the ideal solution whose chemical potential is given by $\mu_0 + k_B T \ln C$. We created an ideal solution by dissolving cholesterol in a hydrocarbon: because solubility is low in the hydrocarbon used, cholesterol molecules are too far apart to interact, and thus cholesterol in a hydrocarbon yields an ideal solution.

We used methyl-β-cyclodextrin (MBCD) as the cholesterol carrier. MBCD molecules bind cholesterol with a fixed stoichiometry, and hence binding of cholesterol to the binding sites of MBCD can be described by a Langmuir isotherm, as was experimentally verified. The isotherm provides the relationship between chemical potential and concentration of cholesterol bound to MBCD in an aqueous phase.
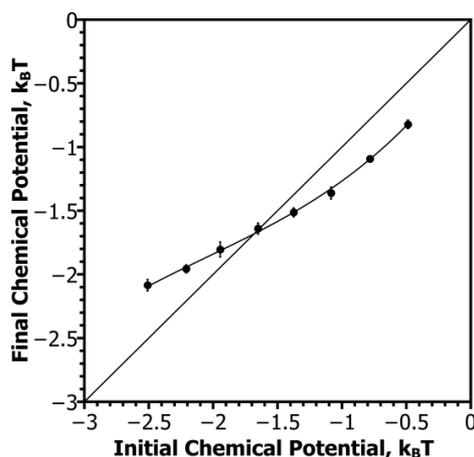
FIGURE 1. The chemical potential of cholesterol in an aqueous solution of MBCD-cholesterol after equilibrating for 15 min (final) vs the chemical potential of cholesterol in the original solution. The intersection of a curve fit through the experimental points and the line of equal initial and final chemical potentials of the solution yields μ_{CH}, the chemical potential of cholesterol in the plasma membrane. For any initial chemical potential, the difference between the experimentally measured final chemical potential and the initial chemical potential is used to obtain the amount of cholesterol that moved into (points above the equilibrium line) or out of (below the line) solution into the cells (MDA-MB-231, a breast cancer cell line).

To determine μ_{CH}, cells in culture are bathed by an aqueous solution that contains MBCD with bound cholesterol. The time for cholesterol to reach equilibrium

between the aqueous solution and plasma membrane is fast, occurring within 15 min. If the cholesterol chemical potential is higher in solution than in the cell membranes, cholesterol will move from solution into cells until the chemical potentials equalize. In contrast, if the chemical potential is lower in the bathing solution, cholesterol will transfer from the cells to MBCD, again equalizing cholesterol chemical potential between plasma membranes and aqueous solution. The only case in which there will be no net transfer of cholesterol is if the cholesterol chemical potential in solution is equal to μ_{CH}. Of course, the likelihood of this happening by chance is nil. Fortunately, one need not experimentally achieve this. The point where a plot of the final chemical potential in solution equals the initial chemical potential (the 45° line of equilibrium) precisely provides the cholesterol chemical potential of the plasma membrane, μ_{CH} (Fig. 1). As a reference, we set the chemical potential of hydrated crystalline cholesterol = 0. Consequently, all measured cholesterol chemical potentials are negative.
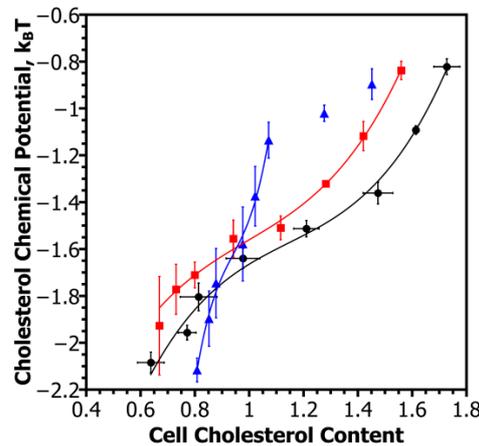
FIGURE 2. μ_{CH}, obtained from experiments illustrated by Fig. 1, is plotted against the total (calculated) cholesterol content of MDA-MB-231 cells. This content is shown as dimensionless, normalized units. The unperturbed content = 1. Note that at all cell densities, an inflection point is present near the cell's natural level of cholesterol. Blue triangles are highest density, red squares are intermediate density, and black circles are the lowest density. Different portions of different curves can be steep or shallow.

The amount of cholesterol that was transferred in reaching equilibrium between the plasma membrane and the aqueous solution is readily obtained from the difference between the amount of cholesterol bound to MBCD at any initial chemical potential and that bound at equilibrium (the final concentration): the final cholesterol content in the plasma membrane is obtained from the initial content and the amount transferred. Knowing this final amount of cholesterol in cells allows the relationship between μ_{CH} and cell cholesterol to be derived (Fig. 2). The dependence of chemical activity on cholesterol concentration in the plasma membrane
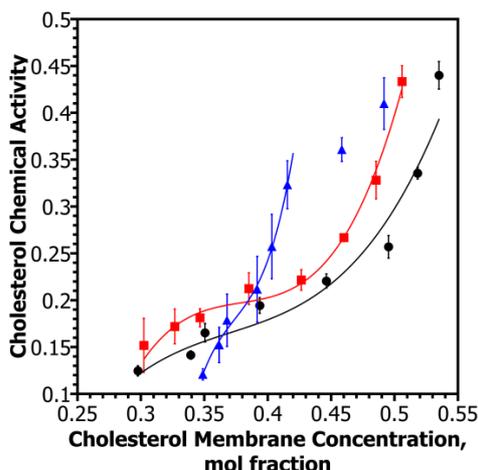
FIGURE 3. The dependence of cholesterol chemical activity on
plasma membrane cholesterol concentration was obtained. We
used the standard values of a plasma membrane cholesterol con-
centration of 40 mol %, and plasma membranes containing 80%
of total cell cholesterol to derive the curves. The overall shape
of a curve for cholesterol activity vs cholesterol concentration in
the plasma membrane depends on the density of cells in culture.
Symbols are the same as for Fig. 2. These curves were calculated
for $\mu_0 = 0$.

is also obtained (Fig. 3). It is striking that cholesterol in the plasma membrane
is not well-approximated by an ideal solution: the activity coefficient of plasma
membrane cholesterol (coefficient = activity/concentration) is only about 0.4 at
the lowest cholesterol concentration, and approaches 1 only at the highest con-
centration, when cholesterol is close to its saturation level. Also, the shapes of
the curves of activity vs. cholesterol content depend on the density (number of
cells/area) of the cells grown in culture. (Here we used breast cancer cells, and
density is easy to vary even though the cells are always confluent because contact
inhibition is absent for cancer cells.) It may be noteworthy that these curves ex-
hibit an inflection point near the natural cell cholesterol content (value 1 in Fig. 2)
or membrane concentration (0.4 mol fraction in Fig. 3) of cholesterol.

This work presents many experimental and theoretical challenges. From the
theoretical viewpoint, one immediate question is: What is implied by the changing
sign of the second derivative of the cholesterol chemical potential, $\frac{\mathrm{d}^2\mu}{\mathrm{d}C^2}$ or equiv-
alently $\frac{\mathrm{d}^2\mu}{\mathrm{d}N^2}$, where N is the number of cholesterol molecules? Model-dependent
interpretations may reveal why the inflection point is situated near the natural,
unaltered cholesterol content. If a model is created to account for this, important
but so far unappreciated biological principles may be uncovered.

References

[1] Ayuyan, AG and Cohen, FS. 2018. *The Chemical Potential of Plasma Membrane Cholesterol: Implications for Cell Biology.* Biophysical J.114:904-918.

Unbalanced optimal transport and quantization

BENEDIKT WIRTH

(joint work with David Bourne, Bernhard Schmitzer)

Formulations of classical optimal transport. The theory of optimal transport (see e. g. [1] for a rigorous introduction) deals with the problem of transporting mass from a given initial mass distribution $\rho_0 \in \mathcal{M}_+(\Omega)$ (where $\Omega \subset \mathbb{R}^n$ shall be a closed bounded Lipschitz domain and $\mathcal{M}_+(\Omega)$ denotes the nonnegative Radon measures on Ω) to a final mass distribution $\rho_1 \in \mathcal{M}_+(\Omega)$ in the most cost-efficient way. The cost for transporting one unit mass from $x \in \Omega$ to $y \in \Omega$ is described by a nonnegative function $c(x, y)$. The original formulation by Gaspard Monge seeks the optimal transport map $T : \Omega \to \Omega$, where $T(x)$ indicates the location which the mass from x shall be transported to,

$$(1) \quad C(\rho_0, \rho_1) = \inf \left\{ \int_\Omega c(x, T(x)) \, \mathrm{d}\rho_0(x) \, \middle| \, \rho_0(T^{-1}(B)) = \rho_1(B) \, \forall B \in \mathfrak{B}(\Omega) \right\}$$

($\mathfrak{B}(\Omega)$ denotes the Borel subsets of Ω). The constraint on T means that after transporting mass ρ_0 by T it equals ρ_1. There are a few conceptual problems with this formulation such as that mass from a point x cannot be split up for the transport. This is remedied by Kantorovich's classical convex formulation seeking a so-called transport plan $\pi \in \mathcal{M}_+(\Omega \times \Omega)$,

$$(2) \quad C(\rho_0, \rho_1) = \min \left\{ \int_{\Omega \times \Omega} c(x, y) \, \mathrm{d}\pi(x, y) \, \middle| \, \begin{array}{l} \pi(B \times \Omega) = \rho_0(B) \\ \pi(\Omega \times B) = \rho_1(B) \end{array} \, \forall B \in \mathfrak{B}(\Omega) \right\},$$

in which $\pi(x, y)$ is interpreted as the mass transported from x to y. Standard Fenchel–Rockafellar duality then yields the Kantorovich–Rubinstein formulation,

$$(3) \quad C(\rho_0, \rho_1) = \sup \left\{ \int_\Omega \alpha \mathrm{d}\rho_0 + \int_\Omega \beta \mathrm{d}\rho_1 \, \middle| \, \alpha(x) + \beta(y) \le c(x, y) \, \forall x, y \in \Omega \right\}.$$

There exist more equivalent formulations (e. g. the flow-based Benamou–Brenier formulation). This allows to always choose the most suitable one for modelling, numerics, or analysis, as will also be exploited below. The choice $c(x, y) = |x - y|^p$ yields an important instance of optimal transport for which $W_p(\rho_0, \rho_1) = \sqrt[p]{C(\rho_0, \rho_1)}$ metrizes weak-* convergence on the space of probability measures.

During the past decades optimal transport theory evolved into a highly active field reaching into different mathematical disciplines. For instance, optimal transport metrics are used in machine learning, properties of partial differential equations (PDEs) and their solutions are investigated using optimal transport-based gradient flows or estimates, and notions of curvature can be defined on nonsmooth spaces using optimal transport. In particular modelling examples are manifold:

- Bio-related *transportation models* often use variants of optimal transport, e. g. modelling nutrient transport or vascular transport networks (see e. g. [1, §4.4.2]).
- Using optimal transport as a metric on molecule distributions (such as the heads and the tails of lipids in a cell membrane) one can derive *biomechanical models* such as a micromodel for cell membrane bending stiffness [4].
- By now it is classical that important PDEs (e. g. the diffusion equation) can be written as *gradient flows* of some entropy with respect to the Wasserstein metric (a Wasserstein-type gradient flow model of tumour growth is found in [2, Ch. 6]).
- The task of optimally discretizing a given measure ρ_0 by a weighted sum of N Dirac masses is known as *quantization* and has various applications; e. g., thinking of ρ_0 as spatial nutrient distribution one can ask how N biological cells would optimally position themselves during competition for resources.
- Several *image and data processing methods* rely on optimal transport, e. g. colour transfer (in which colour histograms of images are masses to be transported) or estimation of molecular motion from a temporal sequence of microscopy images.

Unbalanced transport. If mass is merely transported, ρ_0 and ρ_1 must have identical total mass. So-called "unbalanced transport" also allows mass mismatches between ρ_0 and ρ_1 (e. g. [2]), which meets a strong demand from applications:

- The transported material may change its mass during transport, e. g. moving cells or tissue may grow during the motion.
- The supply $\rho_0(\Omega)$ of a material (e. g. nutrients) may not match the demand $\rho_1(\Omega)$.
- If ρ_0, ρ_1 are measured data, the measurement noise causes spurious mass changes.
- Allowing mass changes increases robustness in transport-based data processing.

The simplest version of unbalanced transport adds a cost $K(\lambda)$ for a mass change by the factor λ, where $K : [0, \infty) \to [0, \infty]$ is convex with $K(1) = 0$. Writing $\frac{\rho}{\mu}$ for the Radon–Nikodym derivative of ρ with respect to μ, (1)-(3) then turn into

$$C(\rho_0, \rho_1)$$

$$= \inf \left\{ \int_\Omega c(x, T(x)) \, \mathrm{d}\rho(x) + \int_\Omega K\left(\tfrac{\rho}{\rho_0}\right) \mathrm{d}\rho_0 + \int_\Omega K\left(\tfrac{\rho \circ T^{-1}}{\rho_1}\right) \mathrm{d}\rho_1 \,\Big|\, \rho \in \mathcal{M}_+(\Omega),\, T : \Omega \to \Omega \right\}$$

$$= \min \left\{ \int_{\Omega \times \Omega} c(x, y) \, \mathrm{d}\pi(x, y) + \int_\Omega K\left(\tfrac{\pi(\cdot, \Omega)}{\rho_0}\right) \mathrm{d}\rho_0 + \int_\Omega K\left(\tfrac{\pi(\Omega, \cdot)}{\rho_1}\right) \mathrm{d}\rho_1 \,\Big|\, \pi \in \mathcal{M}_+(\Omega) \right\}$$

$$= \sup \left\{ \int_\Omega -K^*(-\alpha) \mathrm{d}\rho_0 + \int_\Omega -K^*(-\beta) \mathrm{d}\rho_1 \,\Big|\, \alpha(x) + \beta(y) \leq c(x, y)\, \forall x, y \in \Omega \right\},$$

where $K^*(\gamma) = \sup_{z \in \mathbb{R}} \gamma z - K(z)$ denotes the Legendre–Fenchel conjugate of K. Similarly to classical optimal transport, particular variants of unbalanced transport induce a metric which metrizes weak-* convergence on $\mathcal{M}_+(\Omega)$ [2, Ch. 2]. Current research tries to identify more formulations and feasible numerical schemes as well as fine characterizations of optimal transportat plans (see e. g. [3] and references therein for a characterization of unbalanced W_1-type transport models).

Quantization. As an example of unbalanced transport applications we consider the previously mentioned quantization of a Lebesgue-continuous measure $\rho_0 \in$

$\mathcal{M}_+(\Omega)$ for the case that $c(x,y)$ is an increasing function of $|x-y|$, that is, for fixed $N > 0$ we consider the problem

$$Q(\rho_0) = \min \left\{ C(\rho_0, \rho_1) \,\middle|\, \rho_1 = \sum_{i=1}^{N} m_i \delta_{x_i}, \, m_1, \ldots, m_N \geq 0, \, x_1, \ldots, x_N \in \Omega \right\}.$$

As in classical optimal transport, this allows a geometric reformulation in terms of tiling the domain optimally with Voronoi cells $V_i = \{x \in \Omega \,|\, |x - x_i| \leq |x - x_j| \, \forall j\}$.

Theorem 1. $Q(\rho_0) = \min \left\{ \sum_{i=1}^{N} \int_{V_i} -K^*(-c(x, x_i)) \, dx \,\middle|\, x_1, \ldots, x_N \in \Omega \right\}$.

Proof. 1. Using the notation from the previous paragrph, one first shows existence of an optimal transport map T (Monge formulation) and transport plan π (Kantorovich formulation) for which then necessarily spt$\pi \subset \{(x, T(x)) \,|\, x \in \Omega\}$. *2.* In the optimum, the duality gap between the Kantorovich and the Kantorovich–Rubinstein formulation vanishes, from which one can deduce spt$\pi \subset \{(x, y) \in \Omega \times \Omega \,|\, \alpha(x) + \beta(y) = c(x, y)\}$. Thus, any $x \in \Omega$ with $T(x) = x_i$ satisfies $\alpha(x) + \beta(x_i) = c(x, x_i)$, which together with $\alpha(x) + \beta(x_j) \leq c(x, x_j)$ immediately implies $T^{-1}(x_i) = C_i(\beta) := \{x \in \Omega \,|\, c(x, x_i) - \beta(x_i) \leq c(x, x_j) - \beta(x_j) \, \forall j\}$. *3.* With the above and using $\Omega = \bigcup_{i=1}^{N} C_i(\beta)$ we can now write

$$Q(\rho_0) = \min_{m_i, x_i, \rho, T} \sum_{i=1}^{N} \left[\int_{C_i(\beta)} c(x, x_i) \, d\rho(x) + \int_{C_i(\beta)} K\left(\frac{\rho}{\rho_0}\right) d\rho_0 + m_i K\left(\frac{\rho(C_i(\beta))}{m_i}\right) \right].$$

Explicitly minimizing over m_i and then β yields $m_i = \rho(C_i(\beta))$ and $C_i(\beta) = C_i(0) = V_i$ so that $Q(\rho_0) = \min_{x_i, \rho} \sum_{i=1}^{N} \int_{V_i} c(x, x_i) \frac{\rho}{\rho_0} + K\left(\frac{\rho}{\rho_0}\right) d\rho_0$, which upon optimizing in ρ yields the desired result. $\square$

Again similarly to classical optimal transport, in two spatial dimensions one can even quite precisely estimate the quantization cost $Q(\rho_0)$.

Theorem 2. $Q(\rho_0) = N \int_{H(|\Omega|/N)} -K^*(-c(0, x)) \, dx + O(N^{-1/2})$ *for ρ_0 the Lebesgue measure on $\Omega \subset \mathbb{R}^2$ and $H(A)$ the regular hexagon of area A centred at 0.*

Proof. The upper bound is obtained as the cost $C(\rho_0, \rho_1)$ for a ρ_1 which is constructed as a regular hexagonal lattice of Dirac masses. The lower bound uses Fejes Tóth's result that for any increasing $f : [0, \infty) \to \mathbb{R}$ and l-sided polygon V of area A we have $\int_V f \, dx \geq \int_{V(A,l)} f \, dx$ for $V(A, l)$ the regular l-sided polygon of area A centred at 0 (in our case $f = -K^*(-c(0, \cdot))$). The right-hand side turns out to be convex in A and l so that by Jensen's inequality $Q(\rho_0) = \min_{x_i} \sum_{i=1}^{N} \int_{V_i - x_i} f \, dx \geq N \int_{V(A,l)} f \, dx$, where $A = |\Omega|/N$ and $l = 6$ are the average polygon volume and side number for any Voronoi tesselation. $\square$

One can even characterize the asymptotically optimal point density of ρ_1 for large N if ρ_0 is a spatially varying Lebesgue-continuous measure. In contrast to classical optimal transport, the optimal point density nonlocally depends on the

global mass distribution in such a way that whole regions with positive measure may be completely neglected in favour of regions with higher mass.

REFERENCES

[1] F. Santambrogio, *Optimal Transport for Applied Mathematicians*, Birkhäuser Boston (2015).
[2] L. Chizat, *Transport optimal de mesures positives : modèles, méthodes numériques, applications*, PhD thesis at Univerité Paris-Dauphine, `http://www.dauphine.fr/recherche/soutenances-de-these/detail-dune-soutenance-de-these/soutenance/transport-optimal-de-mesures-positives-modeles-methodes-numeriques-applications.html` (2017).
[3] B. Schmitzer, B. Wirth, *Dynamic Models of Wasserstein-1-Type Unbalanced Transport*, accepted at ESAIM: Control, Optimisation and Calculus of Variations (2018).
[4] M.A. Peletier, M. Röger, *Partial localization, lipid bilayers, and the elastica functional*, Archive for Rational Mechanics and Analyis, **193** (2009), 475–537.

A Hamilton-Jacobi approach for models from evolutionary biology: the case of a time-varying environment

SEPIDEH MIRRAHIMI

(joint work with Susely Figueroa Iglesias)

In this work, we study the evolutionary dynamics of a phenotypically structured population in a time-periodic environment. While the evolutionary dynamics of populations in constant environments are widely studied (see for instance [4, 2, 3, 13, 10]), the theoretical results on varying environments remain limited (see however [8, 11]). The variation of the environment may for instance come from the seasonal effects or a time varying administration of medications to kill cancer cells or bacteria. Several questions arise related to the time fluctuations. Could a population survive under the fluctuating change? How the population size will be affected? Which phenotypical trait will be selected? What will be the impact of the variations of the environment on the population's phenotypical distribution?

The dynamics of phentoypically structured populations subject to selection and mutations, can be modeled by parabolic integro-differential equations or systems (see for instance [9, 4, 1, 3]). The solution of such equations, in the limit of small mutations and in long time, concentrate on one or several Dirac masses (corresponding to dominant traits) which evolve in time.
Here, we study in particular the following Lotka-Volterra type model:

$$(1) \quad \begin{cases} \partial_t n(t,x) - \sigma \Delta n(t,x) = n(t,x)[a(t,x) - \rho(t)], \quad (t,x) \in [0,+\infty) \times \mathbb{R}^d \\ \rho(t) = \displaystyle\int_{\mathbb{R}^d} n(t,x)dx, \\ n(t=0,x) = n_0(x). \end{cases}$$

Here, $n(t,x)$ represents the density of individuals with trait x at time t. The mutations are represented by a Laplace term with rate σ. The term $a(t,x)$ is a time-periodic function, corresponding to the net growth rate of individuals with

trait x at time t. We also consider a death term due to competition between the individuals, whatever their traits, proportional to the total population size $\rho(t)$.

We first prove that, in long time, the solution converges to the unique periodic solution of the problem. Next, we describe this periodic solution asymptotically as the effect of the mutations, σ, vanishes. Using a theory based on Hamilton-Jacobi equations with constraint, we prove that, as the effect of the mutations vanishes, the solution concentrates on a single Dirac mass, while the size of the population varies periodically in time.

When the effect of the mutations are small but nonzero, we provide some formal approximations of the moments of the population's distribution. We then show, via some examples, how such results could be compared to biological experiments [7].

A main part of our work is based an approach based on Hamilton-Jacobi equations with constraint. This approach has been developed during the last decade to study asymptotically the dynamics of populations under selection and small mutations. There is a large literature on this approach. We refer for instance to [4, 12, 10] where the basis of this approach for problems coming from evolutionary biology were established. Note that related tools were already used to study the propagation phenomena for local reaction-diffusion equations [5, 6].

References

[1] Calsina, A. and Cuadrado, S. Asymptotic stability of equilibria of selection-mutation equations. *J. Math. Biol.*, 54(4):489–511, 2007.

[2] Champagnat, N. and Ferrière, R. and Méléard, S. *Individual-based probabilistic models of adaptive evolution and various scaling approximations*, volume 59 of *Progress in Probability*, pages 75–114. Birkhäuser, 2008.

[3] Desvillettes, L., Jabin, P-E., Mischler, S. and Raoul, G. "On selection dynamics for continuous structured populations". *Commun. Math. Sci.*, 6(3):729–747, 2008.

[4] Diekmann, O., Jabin, P-E., Mischler, S., and Perthame, B. "The dynamics of adaptation: An illuminating example and a Hamilton-Jacobi approach". *Theoretical Population Biology*, 67(4):257–271, 2005.

[5] Evans, L.C. and Souganidis, P.E. "A PDE approach to geometric optics for certain semilinear parabolic equations". *Indiana Univ. Math. J.*, 38(1):141–172, 1989.

[6] Freidlin, M. "Limit theorems for large deviations and reaction-diffusion equations". *Ann. Probab.*, 13(3):639–675, 1985.

[7] Ketola, T. and Mikonranta, L. and Zhang, J. and Saarinen, K. and Örmälä, A. M. and Friman, V. P. and Mappes, J. and Laakso, J. Fluctuating temperature leads to evolution of thermal generalism and preadaptation to novel environments. *Evolution*, 67(10):2936–2944, 2013.

[8] Lorenzi, T., Chisholmm R.H., Desvillettes, L. and Hughes, B.D. "Dissecting the dynamics of epigenetic changes in phenotype-structured populations exposed to fluctuating environments". *Journal of Theoretical Biology, Elsevier*, 386:166–176, 2015.

[9] Magal, P. and Webb, G. F. Mutation, selection and recombination in a model of phenotype evolution. *Discrete Contin. Dynam. Syst.*, 6:221–236, 2000.

[10] Mirrahimi, S. *Phénomònes de concentration dans certaines EDPs issues de la biologie.* PhD thesis, Université Pierre et Marie Curie, http://www.math.univ-toulouse.fr/ smir-rahi/manuscrit.pdf., 2011.
[11] Mirrahimi, S., Perthame, B. and Souganidis, P. "Time fluctuations in a population model of adaptive dynamics". *Ann. I.H.Poincaré*, vol. 32, (No. 1):41–58, 2015.
[12] Perthame, B. and Barles, G. "Dirac concentrations in Lotka-Volterra parabolic PDEs". *Indiana Univ. Math. J.*, vol. 7, :3275–3301, 2008.
[13] Raoul, G . *Etude qualitative et numérique d'équations aux dérivées partielles issues des sciences de la nature.* PhD thesis, ENS Cachan, 2009.

Homoenergetic solutions for the Boltzmann equation

Juan J. L. Velázquez

(joint work with Richard D. James, Alessia Nota)

The Boltzmann equation describes the density of particles of a gas in the phase space $f(x, v, t)$. This equation has the form:

$$\partial_t f + v \cdot \nabla_x f = Q[f]$$
$$(1) \qquad = \int_{\mathbb{R}^3} dv_* \int_{S^2} d\omega B(v - v_*, \omega) \left[f_*' f' - f_* f \right], x \in \mathbb{R}^3, v \in \mathbb{R}^3, t > 0$$

where:

$$(2) \qquad v' = v - \left[(v - v_*) \cdot \omega \right] \omega \quad , \quad v_*' = v + \left[(v - v_*) \cdot \omega \right] \omega$$

and:

$$(3) \quad f = f(x, v, t) \quad , \quad f_* = f(x, v_*, t) \quad , \quad f' = f(x, v', t) \quad , \quad f_*' = f(x, v_*', t).$$

In the derivation of (1)-(3) it is assumed that only binary collisions between the gas particles are relevant. The collision kernel $B(v - v_*, \omega)$ depends on the specific form of the interaction between pairs of particles. If the particles interact by means of a power law potential the collision kernel $B(v - v_*, \omega)$ is a homogeneous function of $|v - v_*|$.

There exists a well developed theory of well posedness and a description of the long time behaviour for the solutions of (1)-(3) which are spatially homogeneous, i.e. $f = f(v, t)$. In that case, it can be proved for a large class of collision kernels $B(v - v_*, \omega)$ that the solutions of (1)-(3) approach asymptotically to a Maxwellian distribution:

$$M(v) = \frac{\rho}{(2\pi T)^{\frac{3}{2}}} \exp\left(-\frac{|v - V|^2}{2T} \right) \quad , \quad \rho > 0, \ T > 0, \ V \in \mathbb{R}^3.$$

Maxwellian distributions describe particle distributions of gases in equilibrium situations. However, they cannot be expected to describe velocities in open systems which exchange matter, energy or momentum with the exterior. The mathematical theory of Boltzmann equation in open systems is much less understood than in the case of closed systems.

Nevertheless, there exists a class of solutions of the Boltzmann equation which provide some insight in the dynamics of open systems. These solutions were introduced by Galkin and Truesdell in the $60's$ and they are termed as homoenergetic solutions. They have the form:

$$(4) \qquad f(x,v,t) = g(v - \xi(x,t), t) \quad , \quad w = v - \xi(x,t).$$

From the physical point of view the dispersion of velocities has the same form at every point of the space for these solutions. Only the mean velocity changes from point to point and it might also change in time.

Since the homoenergetic solutions of (1)-(3) depend on a smaller number of variables as the general solution of the Boltzmann equation, the mathematical theory of these solutions is much simpler than the theory of general solutions of the Boltzmann equation. Actually, the well-posedness theory of homoenergetic solutions is (1)-(3) which was developed by Cercignani (cf. [1], [2]) is rather similar to the well posedness theory of homogeneous solutions of (1)-(3).

Actually, some stringent conditions must be assumed for the function $\xi(x,t)$ in order to have solutions of (1)-(3) with the form (4). It turns out that we must have:

$$(5) \qquad \xi(x,t) = M(t)x$$

where $M(t)$ is a 3×3 real matrix for each $t > 0$. Moreover, $M(t)$ must solve:

$$(6) \qquad \frac{dM(t)}{dt} + (M(t))^2 = 0$$

and the function g in (4) satisfies:

$$(7) \qquad \partial_t g(w,t) - M(t)w \cdot \partial_w g(w,t) = Q[g](w,t)$$

The possible asymptotic behaviour of the solutions of (6), (7) has been studied in [3], [4]. We first remark that the general solution of (6) has the form:

$$(8) \qquad M(t) = A(I + At)^{-1}$$

where A is a constant matrix. The long time asymptotics of the functions (8) can be described in detail using the Jordan canonical form of A. This analysis shows that the mapping (5) can yield several types of shear deformations, compression and expansions as well as combination of them. These deformations do not describe the most general possible stretching which can be applied to a gas, but they yield a rather large class of deformations which allow to obtain information about the distribution of velocities for Boltzmann gases under stress in several interesting physical situations.

The long time asymptotics of the solutions of (7) depends on the specific form of $M(t)$ and in the homogeneity properties of the kernel $B(v - v_*, \omega)$. This long time asymptotics is determined by the relative size for large times of the terms

$M\left(t\right)w\cdot\partial_{w}g\left(w,t\right)$ and $Q\left[g\right]\left(w,t\right).$ In the examples studied in [3], [4] we have described examples in which one of the following situations takes place:

(9) $$M\left(t\right)w\cdot\partial_{w}g\left(w,t\right)\ll Q\left[g\right]\left(w,t\right)$$

(10) $$M\left(t\right)w\cdot\partial_{w}g\left(w,t\right)\simeq Q\left[g\right]\left(w,t\right)$$

(11) $$M\left(t\right)w\cdot\partial_{w}g\left(w,t\right)\gg Q\left[g\right]\left(w,t\right)$$

In the first situation the collisions are the most relevant effect. The long time asymptotics of the solutions is then described approximately by Maxwellian distributions for which the temperature changes slowly in time as $t\to\infty$. The temperature can increase or decrease, depending on the specific form of the matrix $M\left(t\right)$. The case (10) is particularly interesting, because there is a balance between collisions and deformations. It has been proved in [3] that there exist self-similar solutions for some choices of $M\left(t\right)$ and collision kernels $B\left(v-v_{*},\omega\right)$ for which (7) admits self-similar solutions for which (10) takes place. These self-similar solutions are non-Maxwellians and fundamental properties like detailed balance which always take place in equilibrium situations do not take place anymore. Finally, some situations in which (11) takes place have been discussed in [4]. In this last situation the particle distributions are non-Maxwellians and are also non-selfsimilar.

References

[1] C. Cercignani, Existence of homoenergetic affine flows for the Boltzmann equation. *Arch. Rat. Mech. Anal.* **105**(4), 377–387, (1989)

[2] C. Cercignani, Shear Flow of a Granular Material. *J. Stat. Phys.* **102**(5),1407–1415, (2001)

[3] R. D. James, A. Nota, J. J. L. Velázquez, Self-similar profiles for homoenergetic solutions of the Boltzmann equation: particle velocity distribution and entropy. *Preprint arXiv:1710.03653* (2017)

[4] R. D. James, A. Nota, J. J. L. Velázquez. Long time asymptotics for homoenergetic solutions of the Boltzmann equation for non Maxwell molecules. *In preparation*

An electroneutral model for ion transport

HUAXIONG HUANG

(joint work with Zilong Song, Xiulei Cao)

The Poisson-Nernst-Planck (PNP) system describes the transport of ions under the influence of both an ionic concentration gradient and an electric field. It is essentially a system coupling diffusion and electrostatics, and the nonlinearity comes from the drift effect of electric field on ions. Such a system and its variants have found extensive and successful applications in biological systems, in particular in the description of ion transport through cells and ion channels [6, 7]. It has also been applied to many industrial fields, such as the semiconductor devices [8] and the detection of poisonous lead by ion-selective electrode [9].

One intriguing feature of this system is the presence of boundary layer (BL) near the boundary of concerned domain, often called Debye layer in literature. A large number of works have been devoted to the BL analysis of PNP systems.

For example, singular perturbation analysis of PNP system has been carried out for narrow ion channels with certain geometric structure [10, 11]. Geometric singular perturbation approach has been developed to investigate the existence and uniqueness of solutions in stationary PNP system [12, 13] as well as the effects of permanent charge and ion size [14, 15]. Recently, Wang et al. [16] have tackled the steady state PNP system with arbitrary number of ion species and arbitrary valences, and have successfully reduced the asymptotic solutions to a single scalar transcendental equation.

In general, the solution consists of two parts, the BL solution in a small neighbourhood of boundary and the bulk solution in the interior region of the domain. In one-dimensional (1D) case, the leading order solution in BL can be constructed either explicitly or in integral form. Based on the BL analysis, effective continuity conditions have been proposed to connect the bulk solution and BL solution, e.g., the continuity of electro-chemical potential in [5]. These effective conditions have been applied to the study of steady states of 1D systems, showing the existence of multiple steady states with piecewise constant fixed charge [4].

In this talk, we present some recent work that systematically derives an electroneutral model with effective conditions that eliminates the need to resolve the boundary layer computationally. These conditions replace the BL region and have potential applications for deriving macroscopic models [3] of bulk region in complicated structures. For example, some macroscopic continuum equations are derived in bulk region for the lens circulation [2, 1], by taking into account the fluxes through membranes with an ad hoc model for the BL effect, so the fluxes calculated there might not be accurate.

The key idea for deriving effective boundary conditions is to bring back the higher order contributions. For the case of Dirichlet boundary conditions, the continuity of electro-chemical potential in [5] can serve as the leading order effective boundary condition. In this talk, we present a higher order effective boundary condition for this case, which can recover the continuity of electrochemical potential at leading order. This condition will be verified by numerical examples and it produces higher-order accuracy in computation. For the case of flux boundary conditions, few people have addressed this issue, because the leading order approximation for flux does not provide a correct effective boundary condition. Mathematically speaking the solution is not unique by using leading order condition, and physically speaking the higher-order contribution accounts for accumulation of ions in BL, which is essential in biophysical processes. These effective conditions are demonstrated in a concrete example of action potential for neuronal axon, where by further simplification the higher-order terms reduce to an equivalent capacitor often adopted in cable models.

References

[1] E. Vaghefi, N. Liu, and P. J. Donaldson, *A computer model of lens structure and function predicts experimental changes to steady state properties and circulating currents*, Biomedical engineering online, **12** (2013), 85.

[2] R. T. Mathias, *Steady-state voltages, ion fluxes, and volume regulation in syncytial tissues*, Biophysical Journal, **48** (1985), 435–448.

[3] H. Huang, J. J. Wylie, and R. M. Miura, *Restricted diffusion in cellular media:(1+ 1)-dimensional model*, Bulletin of mathematical biology, **73** (2011), 1682–1694.

[4] I. Rubinstein, *Multiple steady states in one-dimensional electrodiffusion with local electroneutrality*, SIAM Journal on Applied Mathematics, **47** (1987), 1076–1093.

[5] I. Rubinstein, *Electro-diffusion of ions*, SIAM, 1990.

[6] D. Gillespie and R. S. Eisenberg, *Modified donnan potentials for ion transport through biological ion channels*, Physical Review E, **63** (2001), p. 061902.

[7] T.-L. Horng, T.-C. Lin, C. Liu, and B. Eisenberg, *Pnp equations with steric effects: a model of ion flow through channels*, The Journal of Physical Chemistry B, **116** (2012), 11422–11441.

[8] P. A. Markowich, *The stationary semiconductor device equations*, Springer Science & Business Media, 2013.

[9] J. J. Jasielec, G. Lisak, M. Wagner, T. Sokalski, and A. Lewenstam, *Nernst-planck-poisson model for the description of behaviour of solid-contact ion-selective electrodes at low analyte concentration*, Electroanalysis, **25** (2013), 133–140.

[10] A. Singer, D. Gillespie, J. Norbury, and R. Eisenberg, *Singular perturbation analysis of the steady-state poisson–nernst–planck system: Applications to ion channels*, European journal of applied mathematics, **19** (2008), 541–560.

[11] A. Singer and J. Norbury, *A poisson–nernst–planck model for biological ion channelsan asymptotic analysis in a three-dimensional narrow funnel*, SIAM Journal on Applied Mathematics, **70** (2009), 949–968.

[12] W. Liu, *One-dimensional steady-state poisson–nernst–planck systems for ion channels with multiple ion species*, Journal of Differential Equations, **246** (2009), 428–451.

[13] W. Liu and H. Xu, *A complete analysis of a classical poisson–nernst–planck model for ionic flow*, Journal of Differential Equations, **258** (2015), 1192–1228.

[14] G. Lin, W. Liu, Y. Yi, and M. Zhang, *Poisson–nernst–planck systems for ion flow with a local hard-sphere potential for ion size effects*, SIAM Journal on Applied Dynamical Systems, **12** (2013), 1613–1648.

[15] B. Eisenberg, W. Liu, and H. Xu, *Reversal permanent charge and reversal potential: case studies via classical poisson–nernst–planck models*, Nonlinearity, **28** (2015), 103.

[16] X.-S. Wang, D. He, J. J. Wylie, and H. Huang, *Singular perturbation solutions of steady-state poisson-nernst-planck systems*, Physical Review E, **89** (2014), 022722.

Mathematical modelling and simulation of the early stage of atherosclerosis

MARIA NEUSS-RADU

(joint work with Telma Silva, Willi Jäger, Adelia Sequeira)

Atherosclerosis is the process in which plaques are built up in the walls of arteries, causing stenosis of the lumen, hardening of the arteries and loss of elasticity. This leads to reduction of blood flow through the vessels, blood clot formation (upon rupture of plaques), and break off of blood clots leading to heart attacks or strokes. We consider here only the early stages of atherosclerosis, involving the signaling

processes and the inflammatory response. At this early stage, changes in geometry (e.g. by plaque growth) have no significant impact.

The vascular endothelial cells form an interface between the lumen and the arterial wall, which is composed by three layers: intima, media and adventitia. The endothelial layer is a selective membrane which regulates the homeostasis, controls the exchange of signals (e.g. cytokines), substances (e.g. LDL, water) and cells (e.g. immune cells) between blood and arterial wall. Endothelial dysfunction can be induced e.g., by elevated concentration of low-density-lipoproteins (LDL), low wall shear stress (WSS), free radicals, hypertension or infectious microorganisms, and it leads to a compensatory inflammatory response, see e.g., [3].

The sequence of processes in early atherosclerosis (EA) begins with the accumulation of LDL particles into the intima, due to endothelial dysfunction. Inside the intima, LDL are oxidized, causing the segregation of cytokines and activation of endothelium, leading to an inflammatory reaction. Lumenal monocytes adhere to the activated endothelium, roll along the endothelial cells (EC) surface and finally transmigrate into the intima. There, they differentiate into active macrophages taking up the oxidized LDL (oxLDL), until they become foam cells. In acute inflammation monocytes production is increased due to factor increasing monocytopoiesis (FIM), synthesized and secreted by macrophages. Former contributions to EA are given e.g., in [1, 2].

In this paper, we develop a model of the early atherosclerosis (EA) stage based on new concepts and providing a more detailed understanding. We succeeded in: a) quantifying the LDL accumulation on the EC surface; b) determining the EP to LDL depending on WSS, cytokines and LDL; c) deriving the endothelial permeability (EP) to monocytes as a function of WSS and cytokines; d) taking into account the transport of monocytes on the EC surface (mimicking the monocytes adhesion and rolling) and the increasing in the monocytes influx in the lumen, as result of high concentration of factor increasing monocytopoiesis (FIM); e) coupling between fluid flow in the lumen modeled by the Navier-Stokes system, flow in the vessel wall by Biot system for poroelastic media and the inflammation modeled by convection/chemotaxis-reaction-diffusion equations.

We emphasize that a main focus is set on modeling the functionality of the endothelial layer as a selective interface between lumen and vessel wall. The permeability of this layer to LDL and to monocytes depends on their evolution in the system. This quantity is of central importance for the dynamics of the whole system, motivating the development of the presented model and its simulations, demonstrating the evolutions of relevant factors, at least in a simplified situation.

To give an insight into the mathematical model, let us consider the equations describing the concentration of monocytes. In the lumen, at the endothelium and in the intima, this concentration is denoted by m^l, m^{end} and m^i respectively. In the lumen it is described by

$$(1a) \qquad \frac{\partial m^l}{\partial t} + \nabla \cdot \left(-d_{m^l} \nabla m^l + \mathbf{u}_l m^l \right) = 0$$

with the boundary conditions

$$(1b) \qquad m^l = m_{in}^l + f_m \left(\frac{1}{|\Gamma_{out}|} \int_{\Gamma_{out}} F_{im}^l \, dx \right), \quad \text{at the inflow}$$

$$(1c) \qquad -d_{m^l} \nabla m^l \cdot \mathbf{n}_l = 0, \quad \text{at the outflow}$$

During an acute inflammation the number of circulating monocytes increases controlled by the humoral factor FIM. Thus, in the inlet condition (1b) an extra term f_m representing the additional production of monocytes due to FIM was introduced. f_m is a function of the average of FIM concentration in the lumen, measured at the outlet, chosen to be linear and satisfying $f(0) = 0$.

The total flux of the monocytes from lumen to endothelium can be described by the following transmission condition at the endothelial surface denoted by Γ_{end}:

$$(2) \qquad \left(-d_{m^l} \nabla m^l + \mathbf{u}_l m^l \right) \cdot \mathbf{n}_l = r_m^{acc} \left(m^l - m^{end} \right) \text{ on } \Gamma_{end}.$$

Here, r_m^{acc} is a function that decreases with WSS and increases with cytokines (C_{Mcp}), which can be defined as follows

$$(3) \qquad r_m^{acc} \left(WSS, C_{Mcp} \right) = \frac{r_{m,WSS}^{max}}{1 + WSS/WSS_0} + r_{m,C_{Mcp}}^{max} \frac{C_{Mcp}}{1 + C_{Mcp}}.$$

The motion of the monocytes along the endothelial surface contributes significantly to the opening of the junctions, in order to facilitate the monocytes transmigration. The transport of the monocytes on the EC surface, mimicking the monocytes adhesion and rolling, can be described by the equation

$$(4) \qquad \frac{\partial m^{end}}{\partial t} + \nabla_{\Gamma_{end}} \cdot \left(\mathbf{\Upsilon} m^{end} \right) = r_m^{acc} \left(m^l - m^{end} \right) - P_m \left(m^{end} - m^i \right),$$

where $P_m = P_m \left(WSS, C_{Mcp} \right)$ is the endothelial permeability to monocytes. It is influenced by the inflammatory signals C_{Mcp}, permitting monocytes to leave the circulation and migrate into the focus of injury and by the WSS. The function
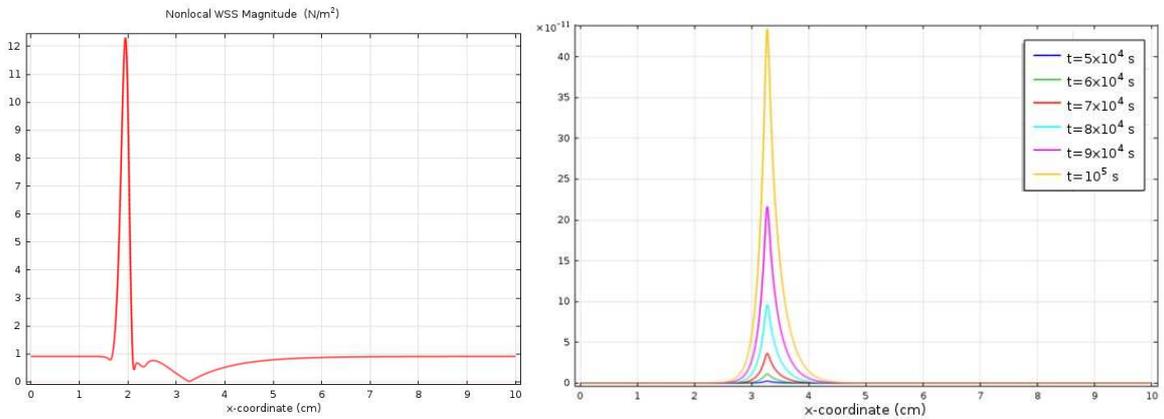

FIGURE 1. The WSS profile for a steady flow (left), and the endothelial permeability to monocytes (right).

$\boldsymbol{\Upsilon}$ is the transport vector field, with the direction of wall shear stress. A more detailed description of $\boldsymbol{\Upsilon}$ is given in [4]. In the intima, the dynamics of monocytes is due to diffusion, reaction and chemotactic migration in the gradient of C_{Mcp}.

Numerical simulations of a simplified early atherosclerosis model in a stenosed vessel were performed in a 2D geometry with experimental data from the literature. As results we mention the following: In Figure 1, we see an increase of the EP to monocytes in the region of low WSS, whereas in Figure 2, the accumulation of monocytes at the site of low WSS magnitude is observed.
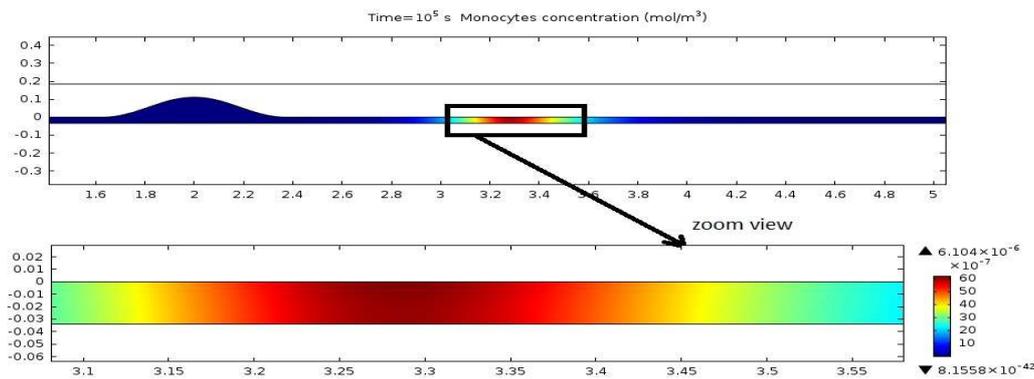
FIGURE 2. Concentration of monocytes inside the intima, for $t = 10^5 \ s$.

REFERENCES

[1] V. Calvez, A. Ebde, N. Meunier and A. Raoult, *Mathematical and numerical modeling of the atherosclerotic plaque formation*, ESAIM Proceedings, **28** (2009), 1-12.
[2] M. Cilla, E. Pea and M. A. Martínez, Mathematical modelling of atheroma plaque formation and development in coronary arteries, *J. R. Soc. Interface*, **11** (2014), 20130866.
[3] R. Ross, *Atherosclerosis - an inflammatory disease*, Massachussets Medical Soc., **340** (1999), 115–126.
[4] T. Silva, W. Jäger, M. Neuss-Radu, A. Sequeira, *Mathematical modelling and simulation of the early stage of atherosclerosis*, submitted.

Multiscale modelling of plant biomechanics and cellular signalling processes

MARIYA PTASHNYK

(joint work with B. Seguin, C. Venkataraman)

Analysis of interactions between mechanical properties and chemical processes, that influence the elasticity and extensibility of plant tissues, is important for a better understanding of plant growth and development. To study the interplay between the mechanics, microscopic structure and the chemistry in plant tissues we derive a microscopic model for plant cell wall biomechanics. Plant cell walls, main feature of plant cells, are composed of cellulose microfibrils imbedded in the wall matrix of pectin and hemicellulose and must be strong to resist high

internal hydrostatic pressure, as well as flexible to permit growth. Pectin, one of the main components of the primary (growing) cell walls, is deposited into the cell wall in a highly methylestrified state, where it is modified by the enzyme pectin-methylesterase (PME) by removing methyl groups. The demethylesterified pectin interacts with calcium ions to produce load bearing cross-links, which reduce cell wall expansion. It is supposed that calcium-pectin cross-linking chemistry is one of the main regulators of plant cell wall elasticity and growth [5].

In the mathematical model we assume that elastic properties of cell walls depend on the chemical processes (interactions between pectin and calcium) and chemical reactions depend on mechanical stresses within the cell walls (the stress within the cell walls can break the load-bearing cross-links). The calcium-pectin chemistry is defined by the following four interactions: (i) demethyl-esterification of pectin by PME, (ii) creation of calcium-pectin cross-links via binding of demethyl-estrified pectin and calcium ions, (iii) breakage of calcium-pectin cross-links under the presence of mechanical stress, (iv) decay of demethyl-esterified pectin, see e.g. [4].

We assume that microfibrils in the cell walls are distributed periodically and have a diameter on the order of ε, characteristic size of the microstructure. Then the domains occupied by microfibrils and the cell wall matrix are defined by

$$\Omega_F^\varepsilon = \bigcup_{\xi \in \mathbb{Z}^2} \left\{ \varepsilon(\hat{Y}_F + \xi) \times (0, a_3) \mid \varepsilon(\hat{Y} + \xi) \subset (0, a_1) \times (0, a_2) \right\} \text{ and } \Omega_M^\varepsilon = \Omega \setminus \overline{\Omega_F^\varepsilon},$$

where $\Omega = (0, a_1) \times (0, a_2) \times (0, a_3)$, with $a_1, a_2, a_3 > 0$, represents a flat section of a cell wall, $\hat{Y} = (0, 1)^2$, $Y = \hat{Y} \times (0, a_3)$, $\hat{Y}_F$ is an open subset, with $\overline{\hat{Y}_F} \subset \hat{Y}$, $\hat{Y}_M = \hat{Y} \setminus \overline{\hat{Y}_F}$, $Y_F = \hat{Y}_F \times (0, a_3)$, and $Y_M = Y \setminus \overline{Y_F}$. The boundary between the wall matrix and microfibrils is denoted by $\Gamma^\varepsilon = \partial\Omega_M^\varepsilon \cap \partial\Omega_F^\varepsilon$.

The calcium-pectin chemistry within the cell wall matrix is described by reaction-diffusion equations for densities of methylestrified pectin $\mathbf{p}_1^\varepsilon$, PME $\mathbf{p}_2^\varepsilon$, demethylestrified pectin $\mathbf{n}_1^\varepsilon$, calcium ions $\mathbf{n}_2^\varepsilon$, and calcium-pectin cross-links b^ε:

$$(1) \quad \begin{cases} \partial_t \mathbf{p}^\varepsilon = \operatorname{div}(D_p \nabla \mathbf{p}^\varepsilon) - \mathbf{F}_p(\mathbf{p}^\varepsilon) \\ \partial_t \mathbf{n}^\varepsilon = \operatorname{div}(D_n \nabla \mathbf{n}^\varepsilon) + \mathbf{F}_n(\mathbf{p}^\varepsilon, \mathbf{n}^\varepsilon) + \mathbf{R}_n(\mathbf{n}^\varepsilon, b^\varepsilon, \mathbf{e}(\mathbf{u}^\varepsilon)) \quad \text{in} \quad \Omega_M^\varepsilon, \ t > 0, \\ \partial_t b^\varepsilon = \operatorname{div}(D_b \nabla b^\varepsilon) + R_b(\mathbf{n}^\varepsilon, b^\varepsilon, \mathbf{e}(\mathbf{u}^\varepsilon)) \end{cases}$$

where $\mathbf{p}^\varepsilon = (\mathbf{p}_1^\varepsilon, \mathbf{p}_2^\varepsilon)$, $\mathbf{n}^\varepsilon = (\mathbf{n}_1^\varepsilon, \mathbf{n}_2^\varepsilon)$, $\mathbf{e}(\mathbf{u}^\varepsilon) = \frac{1}{2}(\nabla \mathbf{u}^\varepsilon + \nabla \mathbf{u}^{\varepsilon\mathrm{T}})$ is the symmetric gradient, $\operatorname{div}(D_m \nabla \mathbf{m}^\varepsilon) = (\operatorname{div}(D_m^1 \nabla \mathbf{m}_1^\varepsilon), \operatorname{div}(D_m^2 \nabla \mathbf{m}_2^\varepsilon))^T$ for $\mathbf{m} = \mathbf{p}^\varepsilon$ or $\mathbf{n}^\varepsilon$, and displacement $\mathbf{u}^\varepsilon$ satisfies the equations of linear elasticity

$$(2) \qquad\qquad \operatorname{div}(\mathbb{E}^\varepsilon(b^\varepsilon, x)\mathbf{e}(\mathbf{u}^\varepsilon)) = \mathbf{0} \qquad\qquad \text{in } \Omega, \ t > 0,$$

with the elasticity tensor defined as $\mathbb{E}^\varepsilon(\xi, x) = \mathbb{E}(\xi, \hat{x}/\varepsilon)$ and the $\hat{Y}$-periodic in y function $\mathbb{E}$ is given by $\mathbb{E}(\xi, y) = \mathbb{E}_M(\xi)\chi_{\hat{Y}_M}(y) + \mathbb{E}_F \chi_{\hat{Y}_F}(y)$ for $\xi \in \mathbb{R}$. Equations (1) and (2) are completed by initial and boundary conditions.

To study mechanical properties of plant cell walls, the macroscopic equations are derived using homogenization techniques of two-scale convergence and periodic unfolding [1]. The macroscopic model for plant cell wall biomechanics has the

same structure as the microscopic equations (1) and (2) with macroscopic diffusion coefficients and macroscopic elasticity tensor determined in terms of solutions of the corresponding 'unit cell' problems. To determine the macroscopic elasticity tensor for the plant cell walls

$$\mathbb{E}_{\text{hom},ijkl}(b) = \fint_Y \left[\mathbb{E}_{ijkl}(b,y) + \big(\mathbb{E}(b,y)\mathbf{e}_y(\mathbf{w}^{ij})\big)_{kl} \right] dy$$

the 'unit cell' problems

$$(3) \quad \begin{cases} \operatorname{div}_y\big[\big(\mathbb{E}_M(b)\chi_{Y_M} + \mathbb{E}_F\chi_{Y_F}\big)(\mathbf{e}_y(\mathbf{w}^{kl}) + \mathbf{b}^{kl})\big] = \mathbf{0} & \text{in } Y, \\ \int_Y \mathbf{w}^{kl}\, dy = \mathbf{0}, & \mathbf{w}^{kl} \text{ is } Y\text{-periodic}, \end{cases}$$

with $\mathbf{b}^{kl} = \frac{1}{2}(\mathbf{b}^k \otimes \mathbf{b}^l + \mathbf{b}^l \otimes \mathbf{b}^k)$ and $k, l = 1, 2, 3$, where $(\mathbf{b}^1, \mathbf{b}^2, \mathbf{b}^3)$ is the standard basis in $\mathbb{R}^3$, are solved numerically [2]. For the microstructure considered here, the macroscopic elasticity tensor $\mathbb{E}_{\text{hom}}(b)$ depends linearly on Young's module of the cell wall matrix, which is a function of the calcium-pectin cross-links density b. Hence it is sufficient to compute $\mathbb{E}_{\text{hom}}(b)$ for two values of b and apply linear interpolation to determine $\mathbb{E}_{\text{hom}}(b)$ for all other values of b. Numerical solutions for the macroscopic model demonstrate heterogeneity in the cell wall displacement due to interactions between mechanical stresses, microstructure, and chemical processes.
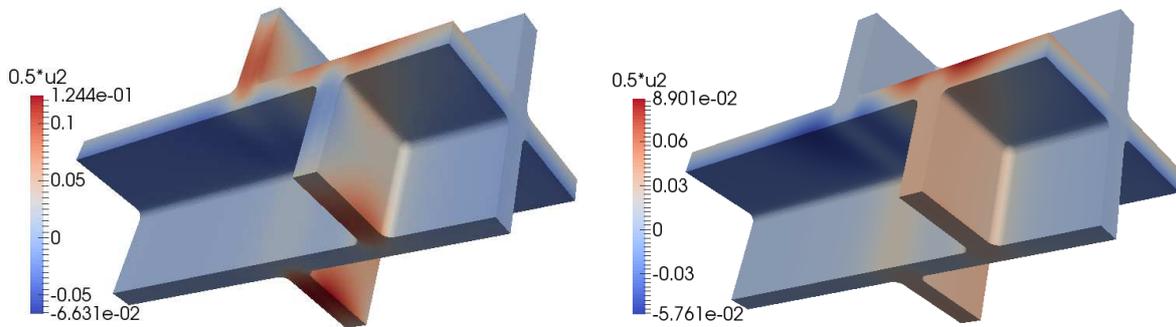
Fig. 1 The displacements in the x_2-direction for different configurations of microfibrils.

In a microscopic model for intercellular signalling processes we consider interactions between signalling molecules diffusing in the extra- and intracellular spaces and receptors and co-receptors localized on the cell membranes. Using multiscale analysis techniques we derive a macroscopic two-scale model for signalling processes on the tissue level, composed of reaction-diffusion equations for signalling molecules c and s in the extra- and intracellular spaces

$$\partial_t c - \nabla \cdot (\mathcal{A}\nabla c) = F_e(c) - \frac{1}{|Y_e|}\int_\Gamma G_e(c, r_f, r_b)d\gamma_y \quad \text{in } \Omega,\ t > 0,$$

$$\partial_t s - \nabla_y \cdot (D_i(y)\nabla_y s) = F_i(s) \quad\quad\quad\quad\quad\quad \text{in } \Omega \times Y_i,\ t > 0,$$

$$D_i(y)\nabla_y s \cdot \nu = G_i(p_a, s) \quad\quad\quad\quad\quad\quad\quad \text{on } \Omega \times \Gamma,\ t > 0,$$

coupled with reaction-diffusion equations for free and bound receptors r_f and r_b and active and inactive co-receptors p_a, p_d

$$\begin{cases} \partial_t r_f = D_f \Delta_{\Gamma,y} r_f - G_e(c, r_f, r_b) \\ \partial_t r_b = D_b \Delta_{\Gamma,y} r_b + G_e(c, r_f, r_b) - G_d(r_b, p_d, p_a) \\ \partial_t p_d = D_d \Delta_{\Gamma,y} p_d - G_d(r_b, p_d, p_a) \\ \partial_t p_a = D_a \Delta_{\Gamma,y} p_a + G_d(r_b, p_d, p_a) - G_i(p_a, s) \end{cases} \quad \text{on } \Omega \times \Gamma,\ t > 0,$$

where Δ_Γ is the Laplace-Beltrami operator on surface Γ, the Lipschitz domain Ω represents a part of a tissue, the 'unit cell' Y and subsets $Y_i \subset Y$ and $Y_e = Y \setminus \overline{Y}_i$ correspond to a rescaled cell surrounded by extracellular space Y_e, see [3]. The macroscopic diffusion matrix $\mathcal{A}$ is defined by

$$\mathcal{A}_{ij} = \fint_{Y_e} \left[D_{e,ij}(y) + \left(D_e(y) \nabla_y w^j \right)_i \right] dy,$$

where

$$-\nabla_y \cdot (D_e(y)(\nabla_y w^j + \mathbf{b}^j)) = 0 \quad \text{in } Y_e, \qquad \int_Y w^j(y) dy = 0,$$

$$-D_e(y)(\nabla_y w^j + \mathbf{b}^j) \cdot \nu = 0 \quad \text{on } \Gamma, \qquad w^j \quad Y-\text{periodic}.$$

Spatial separation in the distribution of signalling molecules in the extra- and intracellular spaces and receptors on the cell membranes triggers formation of patterns on the tissue level.

References

[1] M. Ptashnyk, B. Seguin *Multiscale analysis of a system of elastic and reaction-diffusion equations modelling plant cell wall biomechanics*, ESAIM: M2AN **50** (2016), 593–631.
[2] M. Ptashnyk, B. Seguin *The impact of microfibril orientations on the biomechanics of plant cell walls and tissues: modelling and simulations*, Bull. Math. Biol. **78** (2016), 2135-2164.
[3] M. Ptashnyk, C. Venkataraman *Multiscale analysis and simulations of signalling processes with diffusion*, in preparation, 2018.
[4] S. Wolf, S. Greiner *Growth control by cell wall pectins*, Protoplasma **249** (2012), 169–175
[5] S. Wolf, K. Hématy, H. Höfte *Growth control and cell wall signaling in plants*, Annu. Rev. Plant Biol. **63** (2012), 381–407.

Force generation and contraction of random actomyosin bundles.

DIETMAR OELZ

(joint work with Alex Mogilner (NYU, New York), Boris Y. Rubinstein (Stowers Institute, Kansas City))

The majority of mechanical force generated by cells is caused by the interplay of polar actin filaments and myosin-II molecular motor proteins which generate the force that moves them in the direction indicated by the polarity of the filament. The details of force generation in striated muscle cells are well understood. In non-muscle actomyosin bundles, however, myosin motors and actin filaments are highly disordered and the resulting forces might be either contractile or expansive

(figure 1a). It is therefore not clear what mechanisms promote contractility of non-muscle contractile bundle structures such as the rear bundle in keratocytes, cytokinesis (a crucial substep of cell division) constriction rings and stress fibers.

In [1] we formulate and analyze a minimal mechanism that promotes the contraction of random actomyosin bundles.As a reference experimental system for model formulation and simulations we used the constriction ring which forms in the cortex of eukaryotic cells at the onset of cell division. Its contraction finally leads to the separation of the mother cell into two daughter cells (cytokinesis). We treat the constriction ring as a closed 1D ring of cross-linked actin filaments interspersed with myosin-II motor proteins (figure 1b). The model is the first one to admit the simulation of non-muscle actomyosin contraction on a microscopic scale. Its central part consists of one force balance equation for each of the N actin filaments with index i, velocity v_i and polarity $n_i \in \{-1, 1\}$, which read in the isometric case with fixed radius

$$(1) \quad 0 = \sum_{j=1}^{N} \vartheta_{ij} \underbrace{F_s \left(n_i - \frac{v_i - v_j}{2V_m} \right)}_{\text{Molecular motor force}} - \sum_{j=1}^{N} \underbrace{\eta \, A_{ij} \left(v_i - v_j \right)}_{\text{Cross-linker caused drag friction}} \quad \text{for } i = 1...N \ ,$$

where $\vartheta_{ij} \in \{0, 1\}$ are the coefficients of a connectivity matrix representing connections between actin filaments by molecular motor proteins and A_{ij} represents the length of the region where pairs of filaments overlap and where they are exposed to cross-linking. Furthermore, F_s and V_m are the stall force and free moving velocity of molecular motors and η is the coefficient for cross-linker caused drag friction. The model was derived as a generalized gradient flow and it couples the system (1) to one more equation which relates the contractile tension of the constriction ring σ to the sum of forces transmitted through every possible cross-section of the ring,

$$(2) \quad \sigma = - \sum_{i,j} \vartheta_{ij} F_s \tau_{ij} \left(n_i - \frac{v_i - v_j}{2V_m} \right) + \frac{1}{2} \sum_{i,j} \eta \, A_{ij} \tau_{ij} \left(v_i - v_j \right) \ ,$$

where the coefficients $\tau_{ij} \in \{-1, 0, 1\}$ restrict the summation to the forces transmitted through a specific cross-section.

The result of our numerical experiments (figure **??**) is that in order to contract, actin filaments in the ring have to treadmill, i.e. to elongate at one tip (the "barbed" end) and simultaneously to shorten at other tip (the "pointed" end) and filaments have to be sufficiently crosslinked (figure 1b). The model predicts, in agreement with key experimental observations, a constant rate of contraction. Finally, the model demonstrates that with time pattern formation takes place in the ring worsening the ability of the ring to contract. Therefore the more random actin dynamics are, the higher contractility.

Fluid type continuum models are usually easier to handle and to understand than models which track the fate of single proteins and protein complexes, and their parameters and the quantities they describe are often those which effectively

(A)   (B)
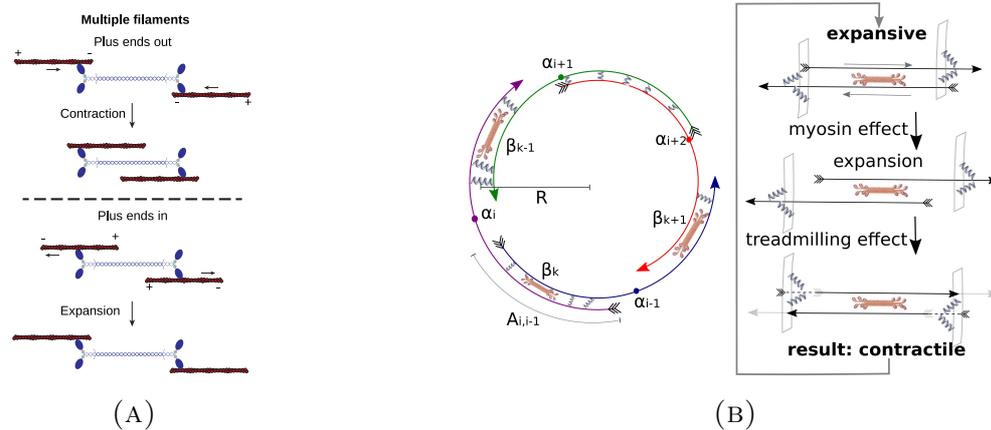
FIGURE 1. Actin filaments are polar having one barbed/plus end
and one pointed/minus end. Myosin-II thick filaments exert forces
that drive them towards the barbed end of actin fibers. As a con-
sequence, actin filaments experience a force that pushes them in
the direction of their pointed ends. (A) Expansive/contractile
effect of myosin-II sliding. Top: for a pair of anti-parallel fila-
ments with barbed/plus ends facing away from a myosin-II dimer
or minifilament, myosin motor activity causes contraction of the
system by pulling the actin filaments closer together. Bottom:
for filaments with barbed/plus ends facing inward, myosin activ-
ity causes expansion by pushing the actin filaments away from
each other (from [2]). (B) Sketch of contractile ring model and
the mechanism of contraction.
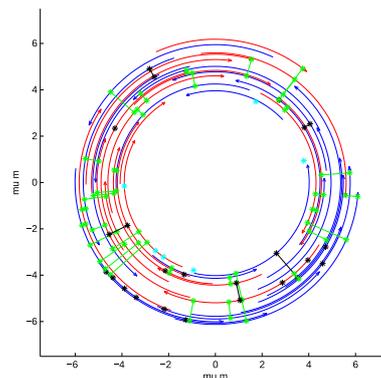
FIGURE 2. Snapshot of the simulation of a contracting cytoki-
nesis ring (side view). Actin filaments are colored according to
their polarity. Myosin thick filaments (green, black, sky-blue) are
colored according to whether they are attached to parallel actin
filaments, anti-parallel ones, or none.

can be observed in experiments. Therefore, in [3], we derive a macroscopic continuum model from the microscopic model (1), (2) for actomyosin contraction. Due to this special procedure its macroscopic parameters are not phenomenological but retain their specific interpretation in terms of aggregated microscopic parameters and quantities.

We consider the limit of dense crosslinking and of actin filaments being much shorter than the length of the bundle/ring, which is exactly what is observed [4]. The singular perturbation analysis reveals the following macroscopic model for the actomyosin ring on the periodic domain $x \in [0, L)$ (here in the special case of fixed length L with isotropic polarity, without initial data),

$$(3) \quad \begin{cases} \partial_t \mu + \partial_x (v\mu) = D_m \partial_{xx} \mu \,, \\[4pt] \partial_t \rho + \partial_x (v\rho - v_{\mathrm{tr}} \, \bar\rho) = D_a \partial_{xx} \rho \,, \\[4pt] \partial_t \bar\rho + \partial_x (v\bar\rho - v_{\mathrm{tr}} \, \rho) = D_a \partial_{xx} \bar\rho \,, \\[4pt] 0 = \zeta \, \rho \, v - F_s \dfrac{l}{2} \partial_x \mu - \eta \dfrac{l^4}{12} \partial_x \left(\rho^2 \partial_x v \right) \,. \end{cases}$$

Drift-diffusion equations for actin filament density $\rho = \rho(t, x)$, where $t > 0$ refers to time, actin filament polarity $\bar\rho = \bar\rho(t, x)$ and myosin motor filament density $\mu = \mu(t, x)$ are coupled to an overdamped momentum equation for the velocity field $v = v(t, x)$. The coefficient v_{tr} is the treadmilling rate at which actin filaments elongate at the barbed/plus ends and shorten at the pointed/minus ends, and ζ describes surface friction. The macroscopic viscosity is given by $\eta \rho^2 l^4 / 12$ where $l > 0$ is the length of actin filaments. The singular perturbation limit also reveals that the macroscopic stress is given by $F_s \, l/2$ representing the bias of myosin binding site positions towards the pointed ends of actin filaments. The fact that the treadmilling rate is strictly positive guarantees that this bias is positive. The actual value of the treadmilling rate, though, does not influence the contractile stress, which is a striking observation.

Analysis and simulations of this model provide many biologically relevant insights and estimates and predict a highly nontrivial pattern formation and traveling wave solutions. This is even more remarkable as recently traveling waves of actomyosin were experimentally observed for the first time [5].

References

[1] D. B. Oelz, B. Y. Rubinstein, and A. Mogilner. A combination of actin treadmilling and cross-linking drives contraction of random actomyosin arrays. *Biophys J*, 109(9):1818–1829, 2015.

[2] A. G. Clark, O. Wartlick, G. Salbreux, and E. K. Paluch. Stresses at the cell surface during animal cell morphogenesis. *Current Biology*, 24(10):R484 – R494, 2014.

[3] D. Oelz and A. Mogilner. Actomyosin contraction, aggregation and traveling waves in a treadmilling actin array. Accepted for publication in Physica D. (preprint available on http://homepage.univie.ac.at/dietmar.oelz/).

[4] D. Vavylonis, J. Wu, S. Hao, B. O'Shaughnessy, and T. D. Pollard. Assembly mechanism of the contractile ring for cytokinesis by fission yeast. *Science*, 319(5859):97–100, 2008.

[5] A. Reymann, R. Boujemaa-Paterski, J. Martiel, C. Gurin, W. Cao, H. F. Chin, E. M. De La Cruz, M. Thry, and L. Blanchoin. Actin network architecture can determine myosin motor activity. *Science*, 336(6086):1310–1314, 2012.

Cell crawling in confined environments without adhesion

Christian Schmeiser

(joint work with G. Jankowiak, D. Peurichard, A. Reversat, M. Sixt)

For many cell types, chemical adhesions are an essential part of their motility machinery, providing the necessary transfer of momentum to the environment. On the other hand it has been shown that leukocyte motility in confined environments is possible in the absence of adhesion [2]. A theoretical explanation of this process is missing.

We have combined an experimental approach, where we observe cell crawling through artificial micro-channels with varying geometry, with a theoretical approach based on a mathematical model, trying to provide a minimal mechanism explaining the experimental observations [1].

The experiments show motility in narrow channels with structured walls of short enough wave lengths (see Fig. 1, top), whereas in channels with flat walls cells are unable to move, although cytoskeletal activity as in moving cells is observed.
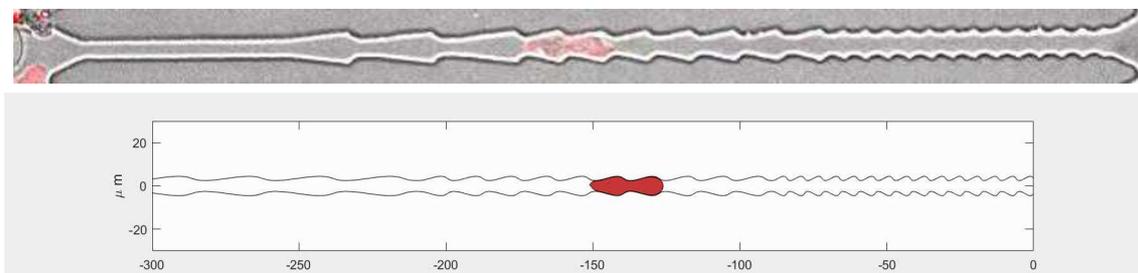
Figure 1. Adhesion-free cell crawling in a micro-channel. Top: experiment. Bottom: simulation

The mathematical model is based on the assumption that the motility is driven by rearward flow of the actin cortex along the cell periphery. We describe the part of the cortex extending between the top and bottom walls of the channel by its projection as a closed curve, which at time t is given by

$$\{X(s,t) : s \in [0,1]\} \subset \Omega \subset \mathbb{R}^2 \qquad \text{with } X(0,t) = X(1,t),$$

where the parameter s is a Lagrangian variable, and Ω describes the channel. The dynamics is modeled by the PDE

$$\mu \partial_t X = P_\Omega \left[v \mathbb{I}_{[s_0, s_1]} \partial_s X + \partial_s \left(\kappa \frac{(|\partial_s X| - 1)_+}{|\partial_s X|} \partial_s X \right) - p \partial_s X^\perp + \mathcal{F}_{comp} \right],$$

where the left hand side describes friction (with friction constant μ) with the surrounding fluid, assumed motionless. The projection P_Ω to the set of admissible velocities is only active for $X \in \partial\Omega$. The first term in the bracket describes net addition (at $s = s_0$) and removal (at $s = s_1$) of cortical actin with speed v by excess polymerization and depolymerization. The next term describes elastic resistance against stretching of the cortex with spring constant κ. An internal excess pressure is denoted by p, causing a force in the outward normal direction. Finally, the force $\mathcal{F}_{comp}$ compensates the momentum created by moving actin material from $X(s_1, t)$ to $X(s_0, t)$. We choose it somewhat distributed around $s = s_0$ and $s = s_1$, satisfying

$$\int_0^1 \mathcal{F}_{comp}(s, t)ds + v(X(s_1, t) - X(s_0, t)) = 0 \,,$$

to provide the appropriate compensation. This guarantees that the center of mass of a cell staying away from the channel walls does not move. Numerical simulations reproduce the qualitative behavior observed in experiments, i.e. no movement in channels with flat walls and movement in structured channels with short enough wave length (see Fig. 1, bottom). More details and an existence analysis can be found in [1].

References

[1] G. Jankowiak, D. Peurichard, A. Reversat, M. Sixt, C. Schmeiser, *Modelling focal adhesion-independent cell migration*, in preparation.

[2] T. Lämmermann, B.L. Bader, S.J. Monkley, T. Worbs, R. Wedlich-Söldner, K. Hirsch, M. Keller, R. Förster, D.R. Critchley, R. Fässler, M. Sixt, *Rapid leukocyte migration by integrin-independent flowing and squeezing*, Nature 453 (2008), 7191:51–55.

Initiation of T cell signalling

Alan D. Rendall

(joint work with Eduardo D. Sontag)

T cells are responsible for recognizing foreign substances (antigens) in our bodies and taking action to eliminate these if necessary. This requires a signalling process where a foreign substance is detected by a receptor molecule on the surface of the cell and this information is transmitted to the nucleus. The machinery involved is a network of chemical reactions. The whole process can take hours or days but here we concentrate on the initiation of the T cell response which only takes a few minutes. It is of central importance for correct T cell function. A system of ordinary differential equations modelling this initial phase was introduced by François et. al. [2] and some aspects of its solutions were studied by numerical and heuristic methods in that paper. Together with Eduardo Sontag we set out to obtain as much information as possible about these solutions by analytical methods. The results are presented in [5] and in what follows we will concentrate on two of the main insights obtained.

In the model of [2] there are two key parameters L and ν, the amount of antigen present and the rate with which an antigen which has bound to the T cell receptor unbinds. One of the unknowns in the ODE system, C_N, indicates that the T cell has been activated. The condition for this is that C_N exceeds a certain threshold. In this context the system is supposed to be in a steady state and the value of C_N in that state is denoted by C_N^*. The quantity of biological interest is then the response function $C_N^* = f(L, \nu)$. In [2] an approximate formula was obtained for the dependence of the function f on L with ν being held constant. In [5] we identified conditions under which we could prove that this formula is an approximation in a suitable sense. As a by-product of the process of precisely formulating and proving this statement we discovered that we could extend the statement to include the dependence on ν. An interesting feature of the dependence of f on L is that it is not monotone. This theoretical prediction of the model has been experimentally confirmed. On the other hand a non-monotone behaviour of f on ν had been seen experimentally but it was believed that this could not be reproduced by the model. In fact these experimental results were controversial but later experiments done in [3] confirmed them. Our formula shows that this feature of f is consistent with the model of [2] if the parameters are chosen correctly. This suggests that the causes of this phenomenon could lie in the first three minutes after the cell encouters its antigen, i.e. in the period which the model is supposed to describe. The most surprising feature of the response function is that in certain regimes it is a decreasing function of L and an increasing function of ν. The approximate expression for f in such a regime is

$$\left(\frac{\phi \beta}{\alpha \gamma S_T} \right)^{N/2} \left(\frac{\kappa R + \nu}{\kappa R} \right)^{N/2 - 1} L^{1 - N/2}$$

and this gives the behaviour of interest when the parameter N is at least three. (All the quantities in this formula other than L and ν are positive parameters in the ODE system.)

The definition of the response function assumes that there is only one steady state for fixed values of the parameters. Our other main result was that this is not always the case. There are parameter values for which there are up to three steady states. This possibility was not considered in [2]. The method of proof is to show that under suitable circumstances steady states are in one-to-one correspondence with positive roots of a certain quartic equation and then to show that the parameters can be chosen so that the number of such roots is three. Whether there are parameters for which more than three steady states exist is an open question. At this point it is appropriate to mention some other models for the initiation of T cell activation in the literature, although no rigorous results are available for those. The model of [2] arose by trying to simplify a much more elaborate model of [1] as much as possible while retaining its explanatory power. The possibility of the existence of multiple steady states was not considered in [1] either. In a model of [4], intermediate in complexity between those of [2] and [1], simulations showed the presence of multiple steady states. In [4] the

authors also studied a stochastic version of their model and found that it could lead to different conclusions from the deterministic model. The reason is that a stable steady state which is inaccessible for the evolution in the deterministic model might be reached by jumping over a barrier in the stochastic model. For comparison, stochastic simulations in [2] did not show any essential differences from the corresponding deterministic model. Multiple steady states were also seen in simulations of a model of intermediate complexity in [6]. In addition stable oscillations were observed. Whether the model of [2] allows periodic solutions is an open question although it was proved in [5] that damped oscillations occur.

References

[1] Altan-Bonnet, G. and Germain, R. N. *Modelling T cell antigen discrimination based on feedback control of digital ERK responses*, PLoS Biol. **3** (2005) (11), e356.

[2] François, P, Voisinne, G., Siggia, E. D., Altan-Bonnet, G. and Vergassola, M. *Phenotypic model for early T-cell activation displaying sensitivity, specificity and antagonism*, Proc. Natl. Acad. Sci. (USA) **110**, (2013) E888–E897.

[3] Lever, M., Lim, H. S., Kruger, P., Nguyen, J., Trendel, N., Abu-Shah, E., Maini, P. K., van der Merwe, P. A. and Dushek, O. 2016 *Architecture of a minimal signaling pathway explains the T-cell response to a million-fold variation in antigen affinity and dose*, Proc. Natl. Acad. Sci. USA **113** (2016), E6630–E6638.

[4] Lipniacki, T., Hat, B., Faeder, J. R. and Hlavacek, W. S. *Stochastic effects and bistability in T cell receptor signalling.* J. Theor. Biol. **254** (2008) 110-122.

[5] Rendall, A. D. and Sontag, E. D. *Multiple steady states and the form of response functions to antigen in a model for the initiation of T cell activation*, R. Soc. open sci. **4** (2017) 70821.

[6] Zheng, Y., Balakrishnan, V., Buzzard, G., Geahlen, R., Harrison, M. and Rundell, A. *Modeling and analysis of early events in T-lymphocyte antigen-activated intracellular-signalling pathways* J. Comp. Appl. Math. **184** (2005) 320–341.

Modelling glioma growth with fully anisotropic diffusion

Thomas Hillen

(joint work with A. Swan, K.J. Painter, C. Surulescu, C. Engwer, M. Knappitsch, A. Murtha)

The human brain has a complex geometric structure consisting of white and gray matter, blood vessels, ventricles, skull etc. It forms a highly anisotropic medium. Glioma in the brain are known to invade along white matter tracks and along other brain structures. Using diffusion tensor imaging (DTI) it is now possible to obtain directional information of the brain geometry [1, 8]. In my talk I will show how this DTI information can be used to parametrize a fully anisotropic diffusion equation for glioma spread [5, 4, 9]. We compare the model to alternative approaches from the literature [2, 7, 6] and we validate the model on clinical data of glioma patients [10]. We discuss the future use in treatment design [10].

REFERENCES

[1] A.L. Alexander, J.E. Lee, M. Lazar, and A.S. Field. Diffusion tensor imaging of the brain. *Neurotherapeutics*, 4(3):316–329, July, 2007.
[2] P.Y. Bondiau, O. Clatz, M. Sermesant, P.Y. Marcy, H. Delingette, M. Frenay, and N. Ayache. Biocomputing: numerical simulation of glioblastoma growth using diffusion tensor imaging. *Physics in Medicine and Biology*, 53:879–893, 2008.
[3] D. Corwin, C. Holdsworth, R.C. Rockne, A.D. Trister, M.M. Mrugala, J.K. Rockhill, R.D. Stewart, M. Phillips, and K.R. Swanson. Toward Patient-Specific, Biologically Optimized Radiation Therapy Plans for the Treatment of Glioblastoma. *PLoS ONE*, 8(11):e79115, 2013.
[4] C. Engwer, T. Hillen, M. Knappitsch, and C. Surulescu. A DTI-based multiscale model for glioma growth including cell-ECM interactions. *J. Math. Biol.* 71(3), 551–582, 2015.
[5] T. Hillen. M^5 mesoscopic and macroscopic models for mesenchymal motion. *J. Math. Biol.*, 53(4):585–616, 2006.
[6] P.R. Jackson, J. Juliano, A. Hawkins-Daarud, R.C. Rockne, and Kristin R. Swanson. Patient-Specific Mathematical Neuro-Oncology: Using a Simple Proliferation and Invasion Tumor Model to Inform Clinical Practice. *Bulletin of Mathematical Biology*, 77:846–856, 2015.
[7] E. Konukoglu, O. Clatz, P.Y. Bondiau, H. Delignette, and N. Ayache. Extrapolating glioma invasion margin in brain magnetic resonance images: Suggesting new irradiation margins. *Medical Image Analysis*, 14:111–125, 2010.
[8] D. Le Bihan, J.F. Mangin, C. Poupon, C.A. Clark, S. Pappata, N. Molko, and H. Chabriat. Diffusion Tensor Imaging: Concepts and Applications. *Journal of Magnetic Resonance Imaging*, 13:534–546, 2001.
[9] K.J. Painter and T. Hillen. Mathematical modelling of glioma growth: the use of diffusion tensor imagining DTI data to predict the anisotropic pathways of cancer invasion. *J. Theor. Biol.*, 323:25–39, 2013.
[10] A. Swan, T. Hillen, J. Bowman, A. Murtha. An Anisotropic Model for Glioma Spread *Bulletin Math. Biol.*, 2017, DOI: 10.1007/s11538-017-0271-8

Modelling Tumor Invasion through Basal Membranes
Luigi Preziosi

Before invading the surrounding tissue, many tumours are contained in membranes that compartmentalize the physiological tissue from the surrounding environment. This quite frequent situation is for instance encountered in breast, ovary, and pancreatic tumours. Actually, when tumours develop remaining inside the membrane they are denoted as *in situ* tumours to distinguish them from invading tumours.

Basal membranes are not solid walls, but are formed by fiber networks that on the one hand allow nutrients and chemical factors to diffuse through very easily, but on the other hand are so tight that cells can not pass through. This is essentially due to the presence of the nucleus that represents the stiffest organelle of the cell. So that, even if the cell can extend protrusions beyond the membrane, its nucleus is trapped by the network, and the cell can not squeeze through.

At a certain stage of development some tumour cells acquire a phenotype characterized by the production of metalloproteinases (MMPs), an enzyme capable to digest the collagen fibers forming the basal membranes. The action of MMPs widens the pores of the fibre network allowing the cell to escape and invade the

surrounding tissue. A similar process also occurs upon encontering several cellular lining, such as the mesothelial layer, and in the processes of intravasation and extravasation of the capillary and lymphatic system, thus representing a fundamental step in the spread of metastases.

Wolf et al. [8] studied the motility of cells in isolation and at the boundary of spherical aggregates as a function of the characteristic pore size of the extracellular matrix (ECM). They identified the existence of a critical pore size for cell migration below which cells stop. This phenomenon, named *the physical limit of migration*, was modelled by Arduino et al. [1] who started from the following multiphase model

$$(1) \qquad \begin{cases} \dfrac{\partial \phi}{\partial t} + \nabla \cdot (\phi \mathbf{v}) = \Gamma \,, \\[2ex] \nabla \cdot \mathbf{T} - \mathbf{M}^{-1} \mathbf{v} = \mathbf{0} \,, \end{cases}$$

associated with a proper constitutive equation describing the stress $\mathbf{T}$ of the cell aggregate that will not be discussed here. In Eq. (1) ϕ is the volume ratio of tumour cells, $\mathbf{v}$ their velocity, Γ is the growth term, and $\mathbf{M}$ is the motility tensor related to the interaction force between cells and the ECM.

The crucial term on which we want to focus here is the motility term, that we will assume isotropic and that on the basis of the experiments in [8] mentioned above might be related to the pore cross section A_m of the ECM through the following relationship

$$(2) \qquad M = \alpha \frac{(A_m(\mathbf{x}) - A_0)_+}{\left(1 + \frac{A_m(\mathbf{x}) - A_0}{A_1}\right)^n} \,,$$

where A_0 is the critical cross-section related to the physical limit of migration. In fact, being $(f)_+ = (f + |f|)/2$ the positive part of f, where $A_m(\mathbf{x}) < A_0$ the motility coefficient vanishes and from the second equation in (1) written as $\mathbf{v} = M \nabla \cdot \mathbf{T}$, it is evident that there is no motion.

The denominator in (2) is introduced to take into account of the existence of an optimal pore size favouring cell migration above which cell speed decreases again, as discussed in [5, 6, 7].

However, the values A_0 is not constant but it is found to depend on some microscopic characteristics of the cells, namely the nucleus size and elasticity, the nuclear membrane stiffness, cell adhesion and traction.

In this respect, Giverso et al. [3, 4] determined a criterium aimed at describing when a cell with a nucleus radius R_n can penetrate a cylindrical microchannel with a section A_p. The criterium involves the dimensionless number $G = \rho_b \alpha_M F / \mu$ that compares the nucleus shear modulus μ with quantities related to the traction forces, namely the density of expressed and activated adhesion modecules, ρ_b, the portion of the surface of contact composed by ECM ligands, α_M, and of course the strength of the traction force F. Hence, large G's correspond, for instance, to larger traction forces, better ability to adhere to the substratum, or softer cell nuclei.

The criterium reads as

(3) $$G < \bar{G} := \frac{a(\tilde{A}_p) + 8\pi\beta b(\tilde{A}_p)}{c(\tilde{A}_p)L(\tilde{A}_p, \tilde{R}_c)},$$

where

$$a(\tilde{A}_p) = \frac{2}{3}\tilde{A}_p + \frac{1}{3\tilde{A}_p^2} - 1, \qquad b(\tilde{A}_p) = \left[\frac{\tilde{A}_p}{2}\left(1 + \frac{\sin^{-1}\sqrt{1-\tilde{A}_p^3}}{\tilde{A}_p^{3/2}\sqrt{1-\tilde{A}_p^3}}\right) - 1\right]^2,$$

$$c(\tilde{A}_p) = \frac{2}{\tilde{A}_p} - 1 + \sqrt{1-\tilde{A}_p}, \quad L(\tilde{A}_p, \tilde{A}_c) = \frac{4\tilde{R}_c^3 - 3\tilde{A}_p - 2\tilde{R}_p^{3/2} - 2 - 2(1-\tilde{A}_p)^{3/2}}{3\sqrt{\tilde{A}_p}}.$$

It can be noticed that the r.h.s. of (3) is a function of the normalized cross section $\tilde{A}_p = A_p/(\pi R_n^2)$ and only through L of $\tilde{R}_c = R_c/R_n$ (where R_c is the cell radius), in addition to the dimensionless parameter $\beta = \lambda_0 R_n/\mu$ that is proportional to the ratio between the stiffness of the nuclear membrane λ_0 and the shear modulus of the nucleus μ.

The criterium allows then to discriminate when multicellular aggregates invade or alternatively are segregated by porous structures, according to microscopic mechanical characteristics of the cells.

Stimulated by the mentioned need to extend the previous approach to the presence of basal membranes, in [2] we used a limit procedure to replace the motion through a layer with specific motility characteristics with an effective thin membrane. In order to explain the result, we can consider the simplest constitutive model for the cell aggregate, $\mathbf{T} = -p(\phi)\mathbf{I}$, so that the mathematical model (1) reduces to

(4) $$\frac{\partial\phi}{\partial t} = \nabla \cdot [\phi M(\mathbf{x})\nabla p(\phi)] + \Gamma.$$

Since at the border of biological tissues the porosity of the ECM can present jumps, the motility M can be discontinuous. Therefore, the usual interface conditions, namely continuity of fluxes and of pressure, must be imposed there.

Considering a thin domain in between two external domains, then when its thickness goes to zero, it is possible to prove that the thin layer can be replaced by a membrane on which the following interface condition need be imposed

(5) $$\tilde{M}[\![\Pi(\phi)]\!] = M\phi\mathbf{n} \cdot \nabla p(\phi),$$

where $\Pi'(\phi) = \phi p'(\phi)$ (primes stand for derivative), $\mathbf{n}$ is the normal to the membrane and it is not important on which side of the membrane the r.h.s. of (5) is evaluated, because it is continuous across the membrane, due to the continuity of flux.

The coefficient $\tilde{M}$ is the effective motility across the membrane. It inherits the same structure as in (2). In particular, for prohibitively small pore cross sections of the ECM, i.e., below the mentioned physical limit of migration, it vanishes yielding the no-flux condition.

It can be noticed that the interface condition (5) is a generalization of the classical Kadem-Katchalsky interface condition. In fact, if $p(\phi) = P \ln \phi/\phi_0$, then Eq. (4) reduces to a standard diffusion equation and the condition (5) reduces to

$$(6) \qquad \qquad \tilde{M}[\![\phi]\!] = M\mathbf{n} \cdot \nabla \phi.$$

In [2] the case of more cell populations was considered yielding a more complicated interface condition.

The model deduced in this way allows to describe the macroscopic invasion or segregation of multicellular aggregates by basal membranes, taking into account of the limitations imposed by the mechanical characteristic of the nuclear envelope and its solid interior material and of the traction ability of the cell.

<div align="center">References</div>

[1] A. Arduino, L. Preziosi, *A multiphase model of tumour segregation in situ by a heterogeneous extra-cellular matrix*, Int. J. Nonlinear Mech. **75** (2015), 22–30.

[2] M.A.J Chaplain, C. Giverso, T. Lorenzi, L. Preziosi, *Interface conditions for a tumour growth model with Basal Membrane*, Math. Med. Biol., submitted.

[3] C. Giverso, A. Arduino, L. Preziosi, *How nucleus mechanics and ECM topology influence the invasion of single cells and multicellular aggregates*, Bull. Math. Biol., in press (doi.org/10.1007/s11538-017-0262-9)

[4] C. Giverso, A. Grillo, L. Preziosi, *Influence of nucleus deformability on cell entry into cylindrical structures*, Biomech. Model. Mechanobiol. **13** (2014), 481–502.

[5] M. Scianna, L. Preziosi, K. Wolf, *A Cellular Potts model simulating cell migration on and in matrix environments* Math. Biosci. Engng., **10** (2013), 235–261.

[6] M. Scianna, L. Preziosi, *Modeling the influence of nucleus elasticity on cell invasion in fiber networks and microchannels*, J. Theor. Biol. **317** (2013), 394-406.

[7] M. Scianna, L. Preziosi, *A cellular Potts model for the MMP-dependent and -independent cancer cell migration in matrix microtracks of different dimensions*, Comp. Mech. **53** (2014), 485–497.

[8] K. Wolf, M. te Lindert, M. Krause, S. Alexander, J. te Riet, A. L. Willis, R. M. Hoffman, C. G. Figdor, S. J. Weiss, P. Friedl, *Physical limits of cell migration: Control by ECM space and nuclear deformation and tuning by proteolysis and traction force*, J. Cell Biol. **201** (2013), 1069–1084.

<div align="center">
On the Dynamics of Fluidic Two-Phase Biomembranes:
Coupling (Navier-)Stokes to Helfrich
</div>

<div align="center">Harald Garcke</div>

<div align="center">(joint work with John W. Barrett and Robert Nürnberg)</div>

Lipid molecules have a hydrophilic head and a hydrophobic tail. They spontaneously aggregate to form a lipid bilayer structure. This biomembrane behaves in normal direction like an elastic material with resistance to bending. In-plane the lipids can move freely which leads to a fluid-like viscous behaviour.

Modeling the membrane idealized as a smooth closed hypersurface $\Gamma \subset \mathbb{R}^d$ Canham [5] and Helfrich[6] introduced the bending energy

$$E_{CH}(\Gamma) = \int_\Gamma (\alpha(\varkappa - \overline{\varkappa})^2 + \overline{\alpha}\mathcal{K})d\mathcal{H}^{d-1}$$

where $\varkappa$ is the mean curvature, $\mathcal{K}$ the Gaussian curvature, α and $\overline{\alpha}$ are bending rigidities and $\overline{\varkappa}$ is the spontaneous curvature.

Arroyo and DeSimone [1] introduced a model for the evolution of biomembranes with the following features. The interior and the exterior of the membrane are modeled as incompressible fluids which in particular leads to conservation of the enclosed volume. The membrane itself is an incompressible fluid which leads to surface area conservation. The fluid flow equations are coupled to the elastic energy via the first variation of the energy

$$\vec{f}_\Gamma = \frac{\delta E}{\delta \Gamma}(\Gamma) = (-\Delta_s \varkappa - (\varkappa - \overline{\varkappa})|\nabla_s \vec{\nu}|^2 + \tfrac{1}{2}(\varkappa - \overline{\varkappa})^2 \varkappa)\vec{\nu}$$

where Δ_s is the surface Laplace operator, ∇_s is the surface gradient, $\nabla_s \vec{\nu}$ is the Weingarten map and $\vec{\nu}$ denotes the exterior unit normal to the region occupied by the interior fluid.

In the model the fluid velocity is assumed to be continuous across the membrane, the membrane is moved in the normal direction with the normal velocity of the bulk fluid and, in addition, the surface Navier-Stokes equations

$$\rho_\Gamma \partial_t^\bullet \vec{u} - \nabla_s \cdot \underline{\underline{\sigma}}_\Gamma = [\underline{\underline{\sigma}}]_-^+ \vec{\nu} + \vec{f}_\Gamma \, , \ \nabla_s \cdot \vec{u} = 0$$

have to hold on Γ. Here ρ_Γ is the surface mass density, $\partial_t^\bullet$ is the material derivative and the surface stress tensor is given as

$$\underline{\underline{\sigma}}_\Gamma = 2\mu_\Gamma \underline{\underline{D}}_s(\vec{u}) - p_\Gamma \underline{\underline{P}}_\Gamma$$

where p_Γ is the surface pressure, μ_Γ is the surface shear viscosity, $\underline{\underline{P}}_\Gamma$ is the projection onto the tangent space and

$$\underline{\underline{D}}_s(\vec{u}) = \tfrac{1}{2}\underline{\underline{P}}_\Gamma(\nabla_s \vec{u} + (\nabla_s \vec{u})^T)\underline{\underline{P}}_\Gamma$$

is the surface rate-of-strain tensor. Furthermore, the term $[\underline{\underline{\sigma}}]_-^+ \vec{\nu}$ is the force exerted by the bulk on the membrane.

In my talk I introduced a finite element approach which has the properties

- volume conservation,
- area conservation,
- energy stability,

on a semi-discrete (continuous in time, discrete in space) level. This approach is hence structure preserving and stable. The last property is due to the fact that the energy stability leads to a priori estimates. We also demonstrated the practicability of the method by several computational results and in particular we were able to show that surface viscosity alone can lead to a transition from tank treading to tumbling for membranes in shear flow.

Finally, I introduced a new model for two-phase fluidic membranes. In this model the above fluid model is supplemented with an additional variable $\mathfrak{c}$ on the membrane which takes the value ± 1 in the pure phases. The energy for two-phase membranes is

$$E(\Gamma, \mathfrak{c}) = \int_\Gamma b(\varkappa, \mathfrak{c}) + \alpha^G(\mathfrak{c})\mathcal{K} + \beta b_{CH}(\mathfrak{c}) d\mathcal{H}^{d-1}$$

with the Cahn–Hilliard energy

$$b_{CH}(\mathfrak{c}) = \tfrac{1}{2}\gamma|\nabla_s\mathfrak{c}|^2 + \gamma^{-1}\Psi(\mathfrak{c})$$

and

$$b(\varkappa, \mathfrak{c}) = \tfrac{1}{2}\alpha(\mathfrak{c})(\varkappa - \overline{\varkappa}(\mathfrak{c}))^2 \,.$$

In particular, the bending energies α, α^G and the spontaneous curvature now depend on the concentration.

Via $\frac{\delta E}{\delta \Gamma}$ the new energy now gives a new forcing term in the fluid equations which in particular leads to a Marangoni type forcing. The concentration $\mathfrak{c}$ solves the convective Cahn–Hilliard surface equation

$$\begin{aligned}
\gamma\partial_t^{\bullet}\mathfrak{c} &= \Delta_s\mathfrak{m}\,, \\
\mathfrak{m} &= -\beta\gamma\Delta_s\mathfrak{c} + \beta\gamma^{-1}\Psi'(\mathfrak{c}) + b_{,\mathfrak{c}}(\varkappa, \mathfrak{c}) + (\alpha^G)'(\mathfrak{c})\mathcal{K}
\end{aligned}$$

which has to hold on Γ. Numerical computations showed effects of the two-phase nature of the membrane like budding and also two-phase membranes tend to remain more deformed after shape deformations through constrictions.

<center>REFERENCES</center>

[1] M. Arroyo and A. DeSimone, *Relaxation dynamics of fluid membranes*, Phys. Rev. E **79** (3) (2009), 031915.

[2] J.W. Barrett, H. Garcke, R. Nürnberg, *Numerical computations of the dynamics of fluidic membranes and vesicles*, Phys. Rev. E **92** (2015), 052704.

[3] J.W. Barrett, H. Garcke, R. Nürnberg, *A stable numerical method for the dynamics of fluidic membranes*, Numer. Math. **134** (4) (2016), 783–822.

[4] J.W. Barrett, H. Garcke, R. Nürnberg, *Finite element approximation for the dynamics of fluidic two-phase biomembranes*, ESAIM: M2AN **51** (6)(2017), 2319–2366.

[5] P.B. Canham, *The minimum energy of bending as a possible explanation of the biconcave shape of the human red blood cell*, J. Theor. Biol. **26** (1970) (1), 61–68.

[6] W. Helfrich, *Elastic properties of lipid bilayers: Theory and possible experiments*, Z. Naturforsch. **28c** (1973), 693–703.

A model for the initiation of pattern generating mechanisms revisited

<center>DIRK HORSTMANN</center>

<center>(joint work with Marcello Lucia)</center>

In 1989 Oster and Murray proposed in [9] a model for the pattern generating of cartilage condensations in the vertebrate limb bud that was later in [7, 8] also connected to the stripe pattern generation mechanisms in the skin of alligator embryos. After some rescaling and some change of notation the model is given by

$$(1) \qquad \begin{cases} n_t &= \Delta n - \nabla \cdot (n\nabla u), \quad x \in \Omega \subset \mathbb{R}^d, t > 0 \\ u_t &= \Delta u - u + \lambda\frac{n}{\gamma+n}, \quad x \in \Omega \subset \mathbb{R}^d, t > 0, \end{cases}$$

where $n(x,t)$ denotes some cell density and $u(x,t)$ an attractant concentration, λ and γ are positive constants and homogeneous Neumann boundary conditions and suitable initial data are assumed to be imposed. Simulations done by P. Grindrod, J. D. Murray and S. Sinha in [2] show that multiple peaks appear as time tends to

infinity. The local existence of a solution for problems like (1) follows (for example) from results by Senba & Suzuki in [11]. The global (in time) boundedness of the solution has been shown (for example) in [6], while the convergence of the solution to a steady state as $t \to \infty$ is established (under some technical assumptions) in [5]. Thus, to get some deeper insights into the final profile of the solution of (1) one should take a closer look at the steady state problem related to (1).

This is exactly what has been done in this talk that reports about some of the results achieved in [5]. The steady state problem related to (1) reduces to a single nonlocal elliptic equation with homogeneous Neumann boundary data given by:

$$(2) \quad -\Delta u + u = \lambda \frac{e^u}{\frac{\omega}{|\Omega|} \int_\Omega e^u + e^u}, \quad \frac{\partial u}{\partial n} = 0 \text{ on } \partial\Omega, \text{ where } \omega = \frac{\gamma|\Omega|}{\int_\Omega n(x,0)dx}.$$

Obviously, the constant function $u_0 = \frac{\lambda}{\omega+1}$ solves trivially the problem. But are there nonconstant solutions of (2) and what do they look like? As a first step one takes a closer look and analyzes the local elliptic Neumann problem:

$$(3) \quad -\Delta u + u = \lambda \frac{e^u}{\gamma + e^u}, \quad \frac{\partial u}{\partial n} = 0 \text{ on } \partial\Omega.$$

We point out, that this is also the local version of the steady state problem related to the following chemotaxis model with volume-filling (compare for example [3]):

$$(4) \quad \begin{cases} n_t &= \Delta n - \nabla \cdot \left(n(1 - \frac{n}{\gamma})\nabla u \right), \\ u_t &= D\Delta u - u + \lambda n. \end{cases}$$

In [3, 4] one can find some plots for the steady state solutions and the time evolution of solutions to (4) for different initial data that show the formation of multiple peaks and, as time prolongs, the coarsening of the peaks. Let us point out that the local problem has also been studied in [1, 2, 10, 12] using completely different approaches, basically bifurcation arguments, in contrast to the techniques used in [5].

We remark that any solution of the local problem (2) satisfies $0 < u < \lambda$ and for each $\lambda > 0$ we have $||u||_{H^1(\Omega)} \leq \lambda^2|\Omega|$.

Now setting $f(s) = s - \lambda\frac{e^s}{\gamma+e^s}$ we see that for all $\lambda, \gamma > 0$ the function $f(s)$ has the following properties:
- $1 \leq \sharp\left(f^{-1}(0)\right) \leq 3$;
- f admits three distinct zeros if and only if

$$\lambda > 4 \quad \text{and} \quad \gamma \in (\gamma_-, \gamma_+), \text{ where } \gamma_\pm = 2e^{\frac{\lambda}{2}}\frac{e^{\pm\frac{1}{2}\sqrt{\lambda(\lambda-4)}}}{\lambda - 2 \pm \sqrt{\lambda(\lambda - 4)}}.$$

Let us denote by z_1, z_2, z_3 the three ordered zeros of f for $\lambda > 4$ and $\gamma \in (\gamma_-, \gamma_+)$. Then, we remark that:
- For $\lambda > 4$: $\max_{s\in[0,\infty)} -f'(s) = \frac{\lambda}{4} - 1$.

- z_1, z_2 are strict local minima of the functional:

$$\mathcal{F}(u) = \int\limits_\Omega |\nabla u|^2 + u^2 \ dx - \lambda \int\limits_\Omega \log\left(\gamma + e^u\right) \ dx.$$

- $\mathcal{F}$ is strictly convex for $\gamma \geq 1$ and $\frac{\lambda}{4} - 1 < \mu_2(\Omega)$, where μ_2 denotes the first nontrivial eigenvalue of the Laplacian with homogeneous Neumann boundary data.
- In one spatial dimension any solution of the local problem has to be constant if $\frac{\lambda}{4} - 1 < \mu_2(I)$ with $I = [0, L]$.

Defining

$$\mathcal{L} = -\Delta + 1, \quad N(u) = \frac{e^u}{\gamma + e^u} \text{ and setting } K(u) := -\mathcal{L}^{-1} \circ N$$

we can rewrite the local problem (3) as

(5) $$(Id + \lambda K)(u) = 0.$$

By the compactness of K and since, at each λ, the set of solutions to (5) is bounded, one remarks that the Leray-Schauder degree of $Id + \lambda K$ is well-defined. In the following its total Leray-Schauder degree is denoted by

$$deg_{LS}(Id + \lambda K) = \sum_{\substack{\text{u is a solution of (5)}}} (-1)^{\nu(u)},$$

where $\nu(u)$ is the Morse index of u. Furthermore, one finds out that

$$deg_{LS}(Id + \lambda K) = 1.$$

Let us assume that we have a given interval $I = [0, L]$ with $L > 0$ large enough. The existence of only one (by reflection two) nontrivial monotone solution of (3) is established by the use of an appropriate time map related to the Neumann problem (3). The following statements about the existence of nontrivial solutions are shown by calculating the Morse indices of the constant solutions and of the unique monotone solution to (3):

- If $\mu_{2k}(I) < -f'(z_2) < \mu_{2k+1}(I)$ holds for some $k \in \mathbb{N}$. For $k = 1$ there exist at least five and for any other $k \in \mathbb{N}$ there exist at least seven solutions for the local problem (3).
- If $\mu_{2k+1}(I) < -f'(z_2) < \mu_{2k+2}(I)$ holds for some $k \in \mathbb{N}$. For $k = 1$ there exist at least seven and for any other $k \in \mathbb{N}$ there exist at least nine solutions for the local problem (3).

Finally, one can turn to the nonlocal problem (2). In a similar way as it has been done for the local problem one can establish the following statements for the nonlocal Neumann problem (2), that (as far as we know) has not been analyzed up to now:

- In one spatial dimension the nonlocal problem (2) admits only the trivial solution $u = \frac{\lambda}{\omega+1}$ if $\frac{\lambda}{4} - 1 \leq \mu_2(I)$, where $I = [0, L]$.

- Let s_0 denote the unique real number satisfying $\omega s_0 e^{s_0} = 1$. If $\lambda - 1 \leq s_0$ then the nonlocal problem (2) admits a unique solution for any dimension.
- In one spatial dimension one can show that, if $\frac{\lambda}{4} - 1 > \mu_2(I)$ and $\lambda \neq \frac{(\omega+1)^2(\mu+1)^2}{\mu\omega}$, where μ denotes an eigenvalue of the Laplacian with homogeneous Neumann boundary data, and $\lambda \neq \frac{4(\omega+1)^2}{\omega}$, then the Morse index of the trivial solution is odd and, therefore, at least one nontrivial solution of (2) has to exist.

References

[1] F.A. Davidson, A.I.M. Savory: Existence and meta-stability of steady states of a model for chemotaxis, Nonlinear Analysis: Real World Applications **17** (2014), pp. 101–113.

[2] P. Grindrod, J. D. Murray, S. Sinha, Steady-State Spatial Patterns in a Cell-Chemotaxis Model IMA Journal of Mathematics Applied in Medicine & Biology **6** (1989), pp. 69–79

[3] T. Hillen and K. Painter, *Volume-filling and quorum-sensing in models for chemotaxis movement*, Canadian Applied Mathematics Quarterly **10** (2002), pp. 501 − 543.

[4] T. Hillen and K. Painter, *A user's guide to PDE models for chemotaxis*, Journal of Mathematical Biology. **58** (2009'), pp. 183 − 217.

[5] D. Horstmann and M. Lucia, *A model for the initiation of pattern generating mechanisms in embryology revisited*, Preprint submitted (2018).

[6] D. Horstmann, *Lyapunov functions and L^p-estimates for a class of reaction-diffusion systems*, Colloquium Mathematicum **87** (2001), pp. 113 − 127.

[7] J. D. Murray, *Modelling the pattern generating mechanism in the formation of stripes on alligators.* In IXth International congress of mathematical physicists, Swansea 1988 (ed. B. Simon, A. Truman & I. M. Davies), pp. 208-213. Bristol: Adam Hilger.

[8] J. D. Murray, D. C. Deeming, D. C. and M. W. J. Ferguson, *Size-Dependent Pigmentation-Pattern Formation in Embryos of Alligator mississippiensis: Time of Initiation of Pattern Generation Mechanism.* Proceedings of the Royal Society of London. Series B, Biological Sciences, Volume 239, Issue 1296 (1990), pp. 279-293.

[9] G. F. Oster and J. D. Murray, *Pattern formation Models and Developmental Constraints*, Journal of Experimental Zoology **251** (1989), pp. 186-202.

[10] R. Schaaf, *Stationary solutions of chemotaxis systems*, Trans. Am. Math. Soc. **292** (1985), pp. 531 − 556.

[11] T. Senba and T. Suzuki, *Applied Analysis*, Imperial College Press, 2004.

[12] X. Wang, Q. Xu, *Spiky and transition layer steady states of chemotaxis systems via global bifurcation and Helly's compactness theorem*, J. Math. Biol. **66** (2013), 1241–1266.

Wrinkling phenomenon in the bidomain model

Giovanni Bellettini

(joint work with S. Amato, M. Paolini, F. Pasquarelli)

The bidomain model originates from a microscopic model describing the electrical properties of the (disjoint) intracellular and extracellular media Ω_i and Ω_e in the cardiac tissue, coupled through the cellular membrane with the addition of a number of variables (Hodgkin-Huxley model), simplified to a single "recovery variable" (FitzHugh-Nagumo), which is neglected here. The bidomain model derives after a homogenization process so that in the end $\Omega_i = \Omega_e = \Omega$, the physical region occupied by the heart. Given $T > 0$, and more generally a smooth bounded connected

open set $\Omega \subset \mathbb{R}^n$, $n \geq 2$, and denoting $u_i = u_{i,\epsilon}$, $u_e = u_{e,\epsilon} : [0, T] \times \Omega \to \mathbb{R}$ the intra and extra cellular electric potentials respectively, the bidomain model can be described with the following weakly parabolic system, of variational nature:

(1)
$$\begin{cases} \epsilon \frac{\partial}{\partial t}(u_i - u_e) - \epsilon \operatorname{div}(M_i \nabla u_i) + \epsilon^{-1} W'(u_i - u_e) = 0, \\ \epsilon \frac{\partial}{\partial t}(u_i - u_e) + \epsilon \operatorname{div}(M_e \nabla u_e) + \epsilon^{-1} W'(u_i - u_e) = 0. \end{cases}$$

Here $\epsilon \in (0, 1)$ is a small positive parameter, W' is the derivative of a double-well potential with minima at ± 1, and M_i, M_e are two symmetric positive definite matrices. The degeneracy of (1) can be understood writing the system as follows:

$$\epsilon \partial_t(B\mathbf{u}) - \epsilon \operatorname{div}\mathbf{q} + \epsilon^{-1}\mathbf{f}(\mathbf{u}) = 0,$$

where $\mathbf{u} = [u_i, u_e]^T$, $\mathbf{q} = [M_i \nabla u_i, -M_e \nabla u_e]^T$, $B = \begin{bmatrix} 1 & -1 \\ 1 & -1 \end{bmatrix}$, the operator div acts componentwise, and $\mathbf{f}([u_i, u_e]^T) = [W'(u_i - u_e), W'(u_i - u_e)]^T$. Although matrix B is singular, problem (1), coupled with (4) below, is well-posed in a suitable sense. We remark that (1) is the "gradient flow" (after a suitable rescaling of time) of the functional

(2)
$$\int_\Omega \left[\frac{\epsilon}{2}(M_i \nabla v \cdot \nabla v + M_e \nabla v \cdot \nabla v) + \epsilon^{-1} W(v - \omega) \right] dx$$

with respect to the degenerate scalar product $((v, \omega), (\eta, \zeta)) \to \int_\Omega (\omega - v)(\zeta - \eta) \, dx$. We refer to [5] for the derivation of the model and its mathematical properties, and for a list of related references.

A crucial role in the description of the electrochemical changes governing the heart beating is played by the *transmembrane potential* $u = u_\epsilon := u_i - u_e$, which typically exhibits a thin transition region of order ϵ which separates the advancing depolarized region where $u \approx 1$ from the one where $u \approx -1$.

We note that one of the two parabolic equations in (1) can be replaced by an elliptic equation, and the system can be equivalently rewritten as

(3)
$$\begin{cases} \epsilon \frac{\partial}{\partial t} u - \epsilon \operatorname{div}(M_i \nabla u_i) + \epsilon^{-1} W'(u) = 0, \\ \operatorname{div}(M_i \nabla u_i + M_e \nabla(u_i - u)) = 0, \\ u = u_i - u_e. \end{cases}$$

System (3) makes more clear the initial and boundary conditions for (1), which are for instance of the form:

(4) $u(0, \cdot) = u_0(\cdot)$ at $\{t = 0\}$, $M_i \nabla u_i \cdot \nu_\Omega = M_e \nabla u_e \cdot \nu_\Omega = 0$ on $[0, T] \times \partial\Omega$,

with u_0 possibly depending on ϵ, ν_Ω the outward unit normal to $\partial\Omega$, and $\cdot$ being the Euclidean scalar product. Our interest here is related to the limit behaviour of the transmembrane potential u, as $\epsilon \to 0^+$. It is worthwhile to recall that the Γ-limit of the sequence of functionals in (2) has been almost characterized [2].

When M_i and M_i are proportional, it can be seen that (1) reduces to a single reaction-diffusion equation for u, a case not of interest in the present discussion.

On the other hand, a nontrivial case is the so-called reciprocal anisotropic ratio, given by $M_i = \text{diag}(\rho, 1)$ and $M_e = \text{diag}(1, \rho)$, $\rho > 0$. We notice that, if we set

$$(5) \qquad (\phi_i(\xi^*))^2 = \alpha_i(\xi^*) := M_i\xi^* \cdot \xi^*, \qquad (\phi_e(\xi^*))^2 = \alpha_e(\xi^*) := M_e\xi^* \cdot \xi^*,$$

where ξ^* denotes a generic covector of the dual $(\mathbb{R}^n)^*$ of $\mathbb{R}^n$, then M_i is the Hessian of $\alpha_i/2$, and $M_i\nabla u_i = T_i(\nabla u_i)$, where $T_i(\xi^*) := \nabla\alpha_i(\xi^*)/2$, and similarly for M_e. In this way, system (1) generalizes to a nonlinear case, i.e., using two *convex* one-homogeneous symmetric functions (called convex anisotropies, not necessarily induced by a scalar product), in place of ϕ_i and ϕ_e. We refer to ϕ_i and ϕ_e in (5) as the case of *linear* convex anisotropies, which is the one we are concerned here.

Remarkably, a non-negligible anisotropy, *not necessarily convex*, and in general nonlinear, occurs in the limit $\epsilon \to 0^+$ of (1), because of the fibered structure of the myocardium. Let us introduce the following function Φ [4], [1], called *combined anisotropy*:[1]

$$(6) \qquad\qquad\qquad \Phi := \left(\frac{1}{\alpha_i} + \frac{1}{\alpha_e}\right)^{-\frac{1}{2}}.$$

It is possible to show [4] that, in the case of reciprocal anisotropic ratio, Φ is convex if and only if $\rho \in [1/3, 3]$. Incidentally, we are not aware of a characterization of those anisotropies that can be obtained combining two convex anisotropies as in (6).

The following *formal* result was proven in [3], to which we refer for the details. *Let be given a smooth boundary ∂E compactly contained in Ω. Suppose that the initial datum $u_0 = u_{0\epsilon}$ is well-prepared around ∂E, in particular $\{u_0 = 0\} = \partial E$. Suppose that $\{\Phi \le 1\}$ (Frank diagram), Φ as in (6), is smooth and uniformly convex. Then, as $\epsilon \to 0^+$, the zero-level set of the solution $u = u_\epsilon$ of (1), (4) converges to the Φ-mean curvature flow starting from ∂E, for sufficiently short times, with an error of order $\mathcal{O}(\epsilon)$.*

The interesting fact is that system (1) remains well-posed even when Φ is not convex, hence when the Φ-mean curvature flow is *ill-posed*. In some sense, system (1), (4) can be considered as one of the possible regularizations[2] of the ill-posed Φ-mean curvature flow. Therefore, it is natural to investigate numerically the behaviour of $\{u = 0\}$ for small values of ϵ, for instance, in the case of reciprocal anisotropic ratio, when $\rho \in (0, 1/3) \cup (3, +\infty)$. Numerical experiments have been performed in [4] for $n = 2$, for large values of $\rho > 3$ and small values of ϵ (say, $\epsilon \approx 0.08$), of the space grid $h = c\epsilon$ with c not too small due to the prohibitive computational cost (say, $c \approx \epsilon/4$) for certain values of time t, looking at the behaviour of the "interface" $\{u(t, \cdot) = 0\}$, taking the unit Euclidean circle ∂E as initial condition. The experiments show the appearence of the wrinkling phenomenon (formation of microstructure). For instance, at time of the order $t \approx 0.02$ one observes the formation of oscillations of wavelength of order ϵ, quickly propagating

---

[1]We observe that the same combination can be done in the more natural context of Minkowski functions of solid symmetric bounded bodies which are star-shaped with respect to the origin.

[2]In view of the instability of the problem, it is not clear whether any reasonable regularization of the Φ-mean curvature flow would lead to the same final evolution.

along only that part of interface having the Euclidean unit normal (Φ-normalized to one) falling in the nonconvex portion of $\{\Phi = 1\}$. This leads to believe that the observed evolution is not the evolution of ∂E by the $\mathrm{co}(\{\Phi \leq 1\})$-curvature flow, $\mathrm{co}(\{\Phi \leq 1\})$ being the convexification of $\{\Phi \leq 1\}$. Next, the oscillations have the tendency to merge, forming longer waves; the wrinkled region tends to disappear, being eroded by the surrounding evolving part. Eventually, the front seems to assume, locally around the discussed region, a form reminiscent to that of the Wulff-shape[3] corresponding to $\mathrm{co}(\{\Phi \leq 1\})$, in this case a strictly convex curve with an angle.

System (1) has been generalized to an arbitrary number of potentials, as well as the formal asymptotics of the corresponding system as $\epsilon \to 0^+$; in this case several nonlinear anisotropies must be combined [1]. Finally, stability of fronts in the bidomain model in $\Omega = \mathbb{R}^2$ has been recently studied in [6].

<div align="center">REFERENCES</div>

[1] S. Amato, G. Bellettini and M. Paolini, *The nonlinear multidomain model: a new formal asymptotic analysis*, "Proceedings of Geometric Partial Differential Equations", CRM Series **15** (2013), (A. Chambolle, M. Novaga, and E. Valdinoci, eds.), Pisa, 33-74.

[2] L. Ambrosio, P. Colli Franzone and G. Savaré, *On the asymptotic behaviour of anisotropic energies arising in the cardiac bidomain model*, Interfaces Free Bound. **2** (2000), 213-266.

[3] G. Bellettini, P. Colli Franzone and M. Paolini, *Convergence of front propagation for anisotropic bistable reaction–diffusion equations*, Asymptotic Anal. **15** (1997), 325-358.

[4] G. Bellettini, M. Paolini and F. Pasquarelli, *Non convex mean curvature flow as a formal singular limit of the non linear bidomain model*, Adv. Differential Equations **18** (2013), 895-934.

[5] P. Colli Franzone, L. F. Pavarino and S. Scacchi, *Mathematical Cardiac Electrophysiology*, MS& A - Modeling, Simulation & Applications, Springer Cham, 2014.

[6] Y. Mori and H. Matano, *Stability of front solutions of the bidomain model*, Comm. Pure Appl. Math. **LXIX** (2016), 2364-2426.

Reporter: Nils Dabrock

---

[3]The Wulff-shape is the dual of the Frank diagram. In this case, the boundary of the original Wulff shape has four transversal intersections and four swallowtails.

Participants

Dr. Abramo Agosti
Dipartimento di Matematica
Politecnico di Milano
Piazza Leonardo da Vinci, 32
20133 Milano
ITALY

Prof. Dr. Davide Ambrosi
Dipartimento di Matematica
Politecnico di Milano
Piazza Leonardo da Vinci, 32
20133 Milano
ITALY

Prof. Dr. Giovanni Bellettini
Dipartimento di Ingegneria
dell'Informazione
e Scienze Matematiche (MAT/05)
Universitá degli Studi di Siena
via Banchi di Sotto, 55
53100 Siena
ITALY

Giulia Bevilacqua
Dipartimento di Matematica
Politecnico di Milano
Piazza Leonardo da Vinci, 32
20133 Milano
ITALY

Dr. Dani Bodor
MRC Laboratory for Molecular Cell
Biology
University College London
Gower Street
London WC1E 6BT
UNITED KINGDOM

Prof. Dr. Fredric Cohen
Department of Physiology
Rush University
Jelke Building
1750 W. Harrison Street
Chicago, IL 60612
UNITED STATES

Nils Dabrock
Fakultät für Mathematik
AG Biomathematik
Technische Universität Dortmund
Vogelpothsweg 87
44227 Dortmund
GERMANY

Dr. Pierre Degond
Department of Mathematics
Imperial College London
Huxley Building
London SW7 2AZ
UNITED KINGDOM

Prof. Dr. Patrick W. Dondl
Abteilung für Angewandte Mathematik
Universität Freiburg
Hermann-Herder-Strasse 10
79104 Freiburg i. Br.
GERMANY

Prof. Dr. Bob S. Eisenberg
Department of Physiology
Rush University
Jelke Building
1750 W. Harrison Street
Chicago, IL 60612
UNITED STATES

Dr. Jan Fuhrmann
Institut für Mathematik
Johannes-Gutenberg Universität Mainz
Staudingerweg 9
55128 Mainz
GERMANY

Prof. Dr. Harald Garcke
Fakultät für Mathematik
Universität Regensburg
93040 Regensburg
GERMANY

Prof. Alain Goriely
Mathematical Institute
University of Oxford
Andrew Wiles Building
Woodstock Road
Oxford OX2 6GG
UNITED KINGDOM

Prof. Dr. Takashi Hiiragi
EMBL Heidelberg
Meyerhofstrasse 1
69117 Heidelberg
GERMANY

Prof. Dr. Thomas Hillen
Centre for Mathematical Biology
University of Alberta
632 Central Academic Building
Edmonton AB T6G 2G1
CANADA

Prof. Dr. Dirk Horstmann
Mathematisches Institut
Universität zu Köln
Weyertal 86 - 90
50931 Köln
GERMANY

Prof. Dr. Huaxiong Huang
Department of Mathematics and
Statistics
York University
4700 Keele Street
North York ON M3J 1P3
CANADA

Prof. Dr. Dagmar Iber
D-BSSE, CoBi
ETH Zürich
Rm. BSB F 6
Mattenstrasse 26
4058 Basel
SWITZERLAND

Prof. Dr. John R. King
School of Mathematical Sciences
The University of Nottingham
University Park
Nottingham NG7 2RD
UNITED KINGDOM

Prof. Dr. Jie Liang
Department of Bioengineering
University of Illinois at Chicago
(MC 563)
820 S. Wood Street
Chicago, IL 60612
UNITED STATES

Prof. Dr. Reinhard Lipowsky
Max-Planck-Institut für Kolloid und
Grenzflächenforschung
Potsdam-Golm Science Park
Am Mühlenberg 1
14476 Potsdam
GERMANY

Prof. Dr. Chun Liu
Department of Mathematics
Pennsylvania State University
University Park, PA 16802
UNITED STATES

Dr. Pei Liu
Department of Mathematics
321 McAllister Building
Pennsylvania State University
University Park, PA 16802
UNITED STATES

Prof. Dr. Michael C. Mackey
Department of Physiology
Centre for Nonlinear Dynamics
McGill University
3655 Prom. Sir William Osler
Montreal QC H3G 1Y6
CANADA

Dr. Sepideh Mirrahimi
Institut de Mathématiques de Toulouse
Université Paul Sabatier
118, route de Narbonne
31062 Toulouse Cedex 9
FRANCE

Prof. Dr. Stefan Neukamm
Fachrichtung Mathematik
Technische Universität Dresden
01062 Dresden
GERMANY

PD Dr. Maria Neuss-Radu
Department Mathematik
Universität Erlangen-Nürnberg
Cauerstrasse 11
91058 Erlangen
GERMANY

Prof. Dr. Dietmar Ölz
Department of Mathematics
University of Queensland
Brisbane Qld. 4072
AUSTRALIA

Klaas Hendrik Poelstra
Fakultät für Mathematik
Technische Universität Dortmund
Vogelpothsweg 87
44227 Dortmund
GERMANY

Prof. Dr. Luigi Preziosi
Dipartimento di Scienze Matematiche
Politecnico di Torino
Corso Duca degli Abruzzi, 24
10129 Torino
ITALY

Dr. Mariya Ptashnyk
Department of Mathematics
University of Dundee
23 Perth Road
Dundee DD1 4HN
UNITED KINGDOM

Dr. Andreas Rätz
Fakultät für Mathematik
Technische Universität Dortmund
AG Biomathematik
Vogelpothsweg 87
44227 Dortmund
GERMANY

Dr. Pierre Recho
Laboratoire de Mathématiques, LIPhy
Institut Fourier
Université de Grenoble I
140 Rue de la Physique
P.O. Box 74
38402 Saint-Martin-d'Hères Cedex
FRANCE

Prof. Dr. Alan Rendall
Fachbereich Mathematik
Universität Mainz
Postfach 3980
55029 Mainz
GERMANY

Davide Riccobelli
Dipartimento di Matematica
Politecnico di Milano
Via Bonardi 9
20133 Milano
ITALY

Prof. Dr. Elisabetta Rocca
Dipartimento di Matematica
Universita di Pavia
Via Ferrata, 1
27100 Pavia
ITALY

Prof. Dr. Matthias Röger
Fachbereich Mathematik
Technische Universität Dortmund
Vogelpothsweg 87
44227 Dortmund
GERMANY

Dr. Angkana Rüland
Max-Planck-Institut für Mathematik
in den Naturwissenschaften
Inselstrasse 22 - 26
04103 Leipzig
GERMANY

Prof. Dr. Arnd Scheel
School of Mathematics
University of Minnesota
127 Vincent Hall
Minneapolis MN 55455-0436
UNITED STATES

Prof. Dr. Anja Schlömerkemper
Institut für Mathematik
Universität Würzburg
Emil-Fischer-Strasse 40
97074 Würzburg
GERMANY

Prof. Dr. Christian Schmeiser
Fakultät für Mathematik
Universität Wien
Oskar-Morgenstern-Platz 1
1090 Wien
AUSTRIA

Dr. Isabelle Schneider
Fachbereich Mathematik und Informatik
Freie Universität Berlin
Arnimallee 7
14195 Berlin
GERMANY

Alexander Schroer
Institut für Angewandte Mathematik
Universität Münster
Einsteinstrasse 62
48149 Münster
GERMANY

Prof. Dr. Angela Stevens
Institut für Analysis und Numerik
Universität Münster
Einsteinstrasse 62
48149 Münster
GERMANY

Dr. Matteo Taffetani
Mathematical Institute
Oxford University
Andrew Wiles Building
Woodstock Road
Oxford OX2 6GG
UNITED KINGDOM

Dr. Britta Trappmann
MPI für molekulare Biomedizin
Röntgenstrasse 20
48149 Münster
GERMANY

Aydar Uatay
Fachbereich Mathematik
Technische Universität Kaiserslautern
Postfach 3049
67653 Kaiserslautern
GERMANY

Prof. Dr. Juan J. L. Velazquez
Hausdorff Center for Mathematics
Institute for Applied Mathematics
Endenicher Allee 60
53115 Bonn
GERMANY

Prof. Dr. Kees J. Weijer
School of Life Sciences
Cell and Developmental Biology
University of Dundee
Dow Street
Dundee DD1 5EH
UNITED KINGDOM

Prof. Dr. Benedikt Wirth
Fachbereich Mathematik und Informatik
Universität Münster
Einsteinstrasse 62
48149 Münster
GERMANY

Prof. Dr. Barbara Zwicknagl
Institut für Mathematik
Sekr. MA 6-4
Technische Universität Berlin
Straße des 17. Juni 136
10623 Berlin
GERMANY